

PHYSICAL CONDITIONS IN THE LOW-IONIZATION COMPONENT OF STARBURST OUTFLOWS: THE SHAPE OF NEAR-ULTRAVIOLET AND OPTICAL ABSORPTION-LINE TROUGHS IN KECK SPECTRA OF ULIRGS

CRYSTAL L. MARTIN¹

University of California, Santa Barbara
Department of Physics and
Santa Barbara, CA, 93106

AND

NICOLAS BOUCHÉ

Max-Planck-Institut Für Extraterrestrische Physik (MPE)
Giessenbachstr. 1, 85748 and
Garching, Germany

Accepted for publication in ApJ.

ABSTRACT

We analyze the physical conditions in the low-ionization component of starburst outflows (in contrast to the high-ionization wind fluid observed in X-rays), based on new Keck/LRIS spectroscopy of partially resolved absorption troughs in near-ultraviolet and optical spectra of Ultraluminous Infrared Galaxies. The large velocity width and blueshift present in seven, atomic transitions indicate a macroscopic velocity gradient within the outflowing gas. The separation of the MgII 2796, 2803 (and FeII 2587, 2600) doublet lines in these data constrains the gas kinematics better than previous studies of the heavily blended NaI 5892, 98 doublet. The identical shape of the MgII 2796 absorption troughs to that of the normally weaker transition at 2803Å (after accounting for emission filling) requires both transitions be optically thick at all outflow velocities. The fraction of the galactic continuum covered by the outflow at each velocity therefore dictates the shape of these absorption troughs. We suggest that the velocity offset of the deepest part of the troughs, where the covering factor of low-ionization gas is near unity, reflects the speed of a shell of swept-up, interstellar gas at the time of blowout. In a spherical outflow, we show that the fragments of this shell, or any clouds that expand adiabatically in rough pressure equilibrium with the hot wind, expand slowly relative to the geometrical dilution; and the covering fraction of low-ionization gas decreases with increasing radius. Our measurement of a covering factor that decreases with increasing velocity can therefore be interpreted as evidence that the low-ionization outflow is accelerating, i.e. absorption at higher velocity comes from gas at larger radii. We also present measurements of $C_f(v)$ in 4 species, place an upper limit of $n_e \lesssim 3000 \text{ cm}^{-3}$ on the density of the outflowing gas, and discuss lower limits on the mass outflow rate.

Subject headings: galaxies: starburst — hydrodynamics — infrared: galaxies — intergalactic medium — ISM: evolution — line: profiles

1. INTRODUCTION

Galactic winds are a key ingredient in cosmological models of galaxy evolution. They transport the nucleosynthetic products of stars into galaxy halos and the intergalactic medium (IGM), thereby shaping enrichment and effective yields. The amount of material ejected from low mass galaxies can significantly reduce the gas mass available for star formation, resulting in lower global efficiencies for star formation that flatten the faint end of the galaxy luminosity function, relative to that of the halo mass function (Somerville & Primack 1999). Some heating mechanism is apparently required in very massive halos in order to make the number of galaxies cutoff more steeply with luminosity than the halo mass distribution does with increasing halo mass. Simulations generally invoke some type of feedback from accreting supermassive black holes, although only the energy scale required distinguishes this feedback from supernova-driven, galactic winds. With mass-loading factors that scale in-

versely with galaxy mass, feedback prescriptions, starburst winds account for the metal enrichment of the intergalactic medium (IGM; e.g., Oppenheimer & Davé 2006).

The scaling relations used for feedback in cosmological simulations are largely motivated by empirical results. Nearby starburst galaxies present hot, extraplanar gas, heated by supernovae (Dahlem et al. 1998; Martin 1999; Strickland et al. 2002; Martin, Kobulnicky, & Heckman 2002). Outflow speeds for low-ionization gas have been measured for much larger samples of nearby galaxies (Heckman et al. 2000; Rupke, Veilleux, & Sanders 2002; Martin 2005; Rupke, Veilleux, & Sanders 2005b; Sato et al. 2009) and composite spectra of distant galaxies (Shapley et al. 2003; Weiner et al. 2009). In the standard dynamical model for the acceleration of this gas, the kinematics of the low-ionization gas reflect properties of a hotter, energetically dominant wind. The hot wind is not a necessary component of the outflow when radiation pressure (on dust grains) accelerates the outflow. Outflow components at vastly different temperatures can only be observed from the X-ray to the infrared for rela-

Electronic address: cmartin@physics.ucsb.edu

¹ Packard Fellow

tively nearby systems. At redshifts $z \gtrsim 0.15$, observations of winds typically detect low-ionization absorption lines and, less commonly, cover strong transitions of OVI, NV, SiIV, and CIV. *Determining what physical information can be reliably extracted from the absorption lines is of paramount importance for understanding any evolution in galactic wind properties over cosmic time.*

For nearby starbursts, the NaI 5892, 5898 lines are the most commonly detected lines from outflows owing to the aperture advantage of ground-based telescopes over satellites. The majority of luminous starburst galaxies present a strong, blueshifted NaI absorption trough (Heckman et al. 2000; Rupke et al. 2002; Martin 2005, 2006; Rupke et al. 2005b; Sato et al. 2009); but the detected fraction in NaI drops to about half for the nearby dwarf, starburst galaxies (Schwartz & Martin 2004). Although the stronger line, NaI 5892, is usually saturated based on its strength relative to the weaker line at 5898Å, the absorption troughs are rarely black. These previous studies have concluded that the NaI absorbers do not completely cover the optical continuum source. The blended absorption troughs have been fitted with the minimum number of velocity components, typically from 1 to 3, required to describe the velocity asymmetry (e.g. Martin 2005, 2006; Rupke et al. 2002, 2005a); and little has been written about the variation of physical parameters with velocity in the outflow. In contrast, the very broad absorption troughs identified as outflows in active galactic nuclei (AGNs) spectra require a velocity-dependent covering factor (Arav et al. 1999a, 2001a; de Kool et al. 2002; Gabel et al. 2003; Scott et al. 2004). Resolving absorption troughs in starburst spectra, and comparing different transitions, can lead to new insight about the nature of the low-ionization component of outflows.

In this paper, we present Keck/LRIS spectroscopy of redshift $z \sim 0.25$ galaxies that partially resolves the NaI 5892, 5897, MgI 2853, MgII 2796, 2803, and FeII 2587, 2600 absorption troughs. We choose Ultraluminous Infrared Galaxies (ULIRGs) due to their high NaI outflow fraction and selected systems at redshifts that provided NaI and near-ultraviolet spectral coverage. The targets are among the most luminous starbursts in the local universe and are classified as ULIRGs, $\log L_{IR} > 12$. Their activity triggers by gas inflow induced by a recent, or on-going, merger (Borne et al. 2000). The wider separation of the MgII doublet lines, 768 km s^{-1} , relative to the NaI doublet, allows direct comparison of the $\lambda 2796$ and $\lambda 2803$ troughs, hereafter the *blue* and *red* troughs respectively. At any location in the outflow, the blue transition has twice the optical depth of the red one; and the covering fraction will necessarily be identical. In contrast to the α -element enrichment measured in the hot wind (Martin, Kobulnicky, & Heckman 2002), the relative abundance of Fe to Mg could be as high as solar in the low-ionization gas, which may be primarily entrained interstellar gas. The optical depth in the FeII line would then be just 1.8 times lower than that in MgII 2803. However, the much weaker FeII 2587 line, $\tau_0(2600) = 3.5\tau_0(2587)$, might be optically thin when the other transitions are saturated. Whether FeII 2587 or NaI 5898 proves to have lower optical depth, and therefore provides the better measurement of ionic column density, depends on the relative

ionization corrections for FeII and NaI.

Our presentation is organized as follows. Section 2 describes the new observations, derives emission-line redshifts, and estimates the sensitivity to outflowing gas. On the first reading, we recommend skipping directly to § 3, where the absorption trough measurements are first presented in a model-independent fashion. Section 3.2 then uses the independent measurements of the trough intensity $I_B(v)$ and $I_R(v)$ to solve directly for optical depth $\tau_R(v)$ and covering fraction $C_f(v)$ as a function of outflow velocity. Since this approach cannot be applied to the majority of the absorption troughs, we introduce a χ^2_ν -fitting method in § 3.3. It differs from previous analyses in terms of the set of physically motivated priors adopted. The advantages are quantitative measurements of the velocity dependence of the covering factor in four species and direct comparison of the limits on gas column density from different transitions. In this way, we establish the relation of the outflow component probed by near-UV resonance lines to that seen in NaI. The connection enables comparison of wind properties over a large redshift range. Our discussion in Section 4 focuses on interpreting the velocity-dependence of the covering fraction. The main results and their implications are summarized in Section 5.

Oscillator strengths and vacuum wavelengths are taken from Morton (1991, 2003) for the optical and near-ultraviolet transitions. We adopt a cosmological model with $H_0 = 70 \text{ km s}^{-1} \text{ Mpc}^{-1}$, $\Omega_0 = 0.3$, and $\Omega_\Lambda = 0.7$ throughout the paper.

2. KECK OBSERVATIONS OF OUTFLOWS IN THE NEAR-ULTRAVIOLET AND OPTICAL

We obtained (rest-frame) near-UV and optical spectroscopy of redshift ~ 0.25 starburst galaxies with LRIS (Oke et al. 1995; McCarthy et al. 1998) on Keck I. The blue channel of LRIS is one of the few optical spectrographs that is efficient down to the atmospheric cut-off in the blue, allowing observations of MgII at $z \gtrsim 0.15$ (for targets directly overhead). The dual-beam design offers simultaneous coverage of NaI absorption and several emission lines in the red channel. Due to the low density of bright galaxies at these redshifts, the spectra must be obtained one at a time.

Galaxies were chosen from the IRAS 1 Jy survey of ULIRGs (Kim & Sanders 1998), which contains 118 ULIRGs with $F_{60} > 1 \text{ Jy}$, based on apparent magnitude and airmass at the time of our runs. Ultraluminous Infrared Galaxies are extremely rare at the present epoch but offer the closest local analog of the IR-luminous galaxy population that dominates the cosmic star formation rate density at redshifts greater than 0.7 (Le Floc'h et al. 2005). The high dust content absorbs much of the stellar luminosity and emits this energy as thermal radiation in the infrared.

Table 1 lists some properties of the galaxies whose spectra are presented in this paper. The infrared luminosities of the galaxies observed range from $\log L_{IR} = 12.31 - 12.81$ with mean $\log L_{IR} = 12.58$, which is more luminous than the mean of the Martin (2005, 2006) sample. The AGN fraction is higher in brighter ULIRGs (Veilleux et al. 1999); and two of the five ULIRGs in the sample are spectroscopically classified as AGN (2 LINERs and 2 Sey 2's). The more recent

Kewley et al. (2006) division of these optical-emission-line ratios into excitation types classifies FSC 0039-13 as a composite starburst-AGN, FSC 1009+47 as a Seyfert 2, FSC 1407+05 at the Seyfert/LINER boundary, FSC 1630+15 at the LINER/Composite boundary, and FSC 2349+24 as a Seyfert 2. Among our five targets, FSC 2349+24 clearly presents the strongest AGN signatures, but AGN contribute less than half of the bolometric luminosity in the other four ULIRGs (Veilleux et al. 2009a). Among our five targets, FSC 2349+24 clearly presents the strongest AGN signatures. Rupke et al. (2005d) found little difference in NaI wind kinematics between HII, LINER, and Sey 2 ULIRGs; only the Sey 1's showed faster outflows. Hence, we expect these outflows are driven primarily by the starburst rather than the AGN. The far-infrared colors are all cooler than the standard demarcation, $F(25\mu m)/F(60\mu m) > 0.2$, used to identify warm ULIRGs (Kim et al. 1998), which also suggests the total luminosity is starburst dominated. The total infrared luminosities correspond to upper limits on the star formation rates from $SFR \sim 207 - 653 M_{\odot} \text{ yr}^{-1}$ or $\sim 352 - 1110 M_{\odot} \text{ yr}^{-1}$, respectively, for the Chabrier or Salpeter initial mass functions.

2.1. Data Acquisition and Reduction

Longslit spectra were obtained with LRIS (Oke et al. 1995) and LRISb (McCarthy et al. 1998) on 2004 January 26, 2004 March 16-17, 2007 October 6, and 2007 November 1. Clouds and high humidity limited the exposure times on all of these nights. We present the five highest quality spectra obtained from the combined data.

The position angle of the longslit was selected to cover both nuclei of FSC 1009+47 and FSC 2349+24. The atmospheric dispersion compensator, which was installed on LRIS in spring 2007, was used for the 2007 observations. Care was taken with the 2004 observations to observe the targets when the slit PA was near the parallactic angle.

The dual beam spectrograph was configured with the D560 dichroic, a 1200-l grism blazed at 3400Å in the blue arm (LRISb) and a 1200-l grating blazed at 7500Å in the red arm. The grating tilt for each target was tuned to cover the $H\alpha + [\text{NII}]$ emission lines as well as the NaI absorption and HeI 5876 emission line. The blue spectra cover the MgII 2796, 2803 doublet, the MgI 2853 line, and the FeII 2587, 2600 doublet. The slit width was chosen based on the atmospheric seeing. The resolution (for a source filling the slit) ranged from 110 km s⁻¹ on the 2004 March run to 160 km s⁻¹ on the 2007 November run and is listed in Table 2. The size (FWHM) of the galaxies along the slit exceeded the slit width.

Fixed-pattern noise was removed using software scripts that called IRAF tasks.² The blue spectra were flat-fielded with twilight sky frames, normalized by the sky spectrum. The red spectra were flatfielded using an internal (spectroscopic) exposure of a quartz lamp. A dispersion solution was fitted to the vacuum wavelengths of the arc lamp lines as a function of detector coordinate. The root mean square error in the dispersion so-

See Figure 1 on p.22

FIG. 1.— Normalized intensity vs. velocity, where the velocity is relative to the systemic velocity determined from emission lines.

lution for the blue (red) spectra was 0.05 (0.07) Å. Application of a small, additive shift, up to a couple tenths of an angstrom, registered the wavelengths of night sky emission lines with their values in a telluric-line spectrum (Hanuschik 2003) smoothed to our spectral resolution and transformed to vacuum wavelengths (using the Edlen formula). We attribute these corrections to shifts in the dispersion solution with airmass and rotator angle. The correction to the Local Standard of Rest (LSR) was computed for each observation using the IRAF task RV-CORRECT. All the offsets were less than 30 km s⁻¹. Since we are only concerned with relative velocities, the corrections to LSR were not applied to the data.

We rectified the two-dimensional spectral images, using the dispersion solution and traces of a standard star stepped along the longslit, and then extracted an integrated galaxy spectrum for each target. These spectra have $SNR \sim 5 - 10$ per pixel as shown in Table 2. Additional, lower quality spectra were extracted for the distinct continuum sources within FSC 1009+47, FSC 1407+05, and FSC 2349+24. After subtraction of the median sky intensity at each wavelength, significant residuals from strong night-sky emission lines remained in the red spectra near the NaI line in FSC 1009+47, 1407+05, and 1630+15. Variance spectra were extracted for each target prior to sky subtraction and flux calibration. The variance vectors were later scaled by a multiplicative factor that made the uncertainties in the intensity consistent with the measured standard deviation in the extracted, target spectra.

Observations of multiple, standard stars determined the relative sensitivity with wavelength. The data were flux calibrated using this sensitivity function and then normalized by a fitted continuum. The error in continuum placement is negligible around NaI, MgI, and MgII; but the blending of stellar absorption lines washes out the true continuum level at shorter wavelengths. To identify bandpasses near FeII 2587, 2600 that likely reach the true continuum level, we compared high-resolution, synthesized spectra models of stellar populations to copies smoothed to 100 km s⁻¹ resolution. We fitted a first or second order cubic-spline through these bandpasses as well as the broad bandpasses near the MgI and MgII lines. The resulting error in the continuum level near FeII depends on the star formation history. The severe blanketing in older bursts requires actual fitting of reddened, model spectra. This level of sophistication was unnecessary, however, because these near-UV spectra are bluer than the $t > 100$ Myr burst models; and we confidently rule out old, burst models for the continuum. The population synthesis models indicate either continuous star formation or a burst within the past 100 Myr. Repeated fitting trials indicate the uncertainty in the continuum level around FeII was 1 to 5%.

For a typical line width of 470 km s⁻¹ FWHM, we detect a rest-frame equivalent width $W_r(5\sigma) \approx 1.52\text{\AA}(5/SNR_{pix})(\Delta v/470 \text{ km s}^{-1})^{0.5}$ in the red spectra at the 5 σ significance level. A typical 5 σ sensitivity limit for the blue spectra is $W_r(5\sigma) \approx 0.92\text{\AA}(5/SNR_{pix})(\Delta v/470 \text{ km s}^{-1})^{0.5}$.

² IRAF is distributed by the National Optical Astronomy Observatory, which is operated by the Association of Universities for Research in Astronomy (AURA) under cooperative agreement with the National Science Foundation.

2.2. Sensitivity of Spectra to Physical Properties

We measured redshifts from recombination lines of H and He and forbidden lines of singly-ionized N and S. These lines all fall in our red spectra. The dispersion solution ties both the blue and the red spectra to the *vacuum wavelengths* of night sky emission lines. These redshifts agree with the previous measurements of Kim & Sanders (1998). Our independent check is important because that work used the NaI absorption line in the redshift estimate; and we will show that the NaI kinematics differ significantly from that of the recombination lines.

The sensitivity of the seven metal lines to outflowing gas depends on the relative abundances of the elements, the oscillator strengths of the transitions, the dust depletion, and the ionization corrections. In the limit of comparable ionization corrections for all species, the optical depth in the MgI 2853 line would be the largest for solar-abundance ratios. The MgII lines have lower oscillator strengths, and the cosmic abundances of Fe and Na are lower. Our typical detection limit for MgI corresponds to a minimum hydrogen column density,

$$N(HI) = 1.62 \times 10^{17} \text{ cm}^{-2} (N(Mg)/N(MgI)) \times (5/SNR) \frac{1.25}{1+z} (\Delta v/470 \text{ km s}^{-1})^{0.5}. \quad (1)$$

Under the same conditions, the NaI 5898 line optical depth would be slightly lower than the weakest FeII line, but whether either transition is optically-thin depends on the relative ionization correction, where

$$\frac{\tau_0(\text{FeII } 2587)}{\tau_0(\text{NaI } 5898)} = 1.41 \frac{\chi(\text{FeII})}{\chi(\text{NaI})}. \quad (2)$$

The NaI 5898 line can, in principle, provide the best measurements of an ionic column density in the outflow, but interpretation is complicated by the blending with the NaI 5892 transition, the ionization correction, and depletion of Na by dust grains. The FeII transitions with the lowest oscillator strengths lie blueward of the atmospheric cut-off for nearby galaxies, and their measurement will likely lead to the best estimates of mass column density.

3. MEASURED PROPERTIES OF LOW-IONIZATION OUTFLOWS

Figure 1 shows the absorption troughs on a velocity scale. The high spectral resolution, relative to the broad troughs, allows us to compare the shape of the absorption troughs among seven transitions. The centroids of the H α and [NII] emission lines lie at the systemic velocity by construction. The spectra of all five galaxies present broad absorption troughs in the NaI and MgII doublets. The spectrum of FSC 0039-13 has the best SNR near the MgI 2853, FeII 2600, and FeII 2587 lines; but these transitions are detected in all the spectra except for FSC 2349+24. The FeII 2587, 2600 lines lie shortward of $\lambda 3200$ for FSC 2349+24, and the SNR is severely compromised by atmospheric attenuation. In Figure 1, the two Seyfert 2 galaxies in the sample, FSC 1407+05 and FSC 2349+24, present MgII in emission. Some He I emission is present near the NaI doublet in all the spectra and is most prominent in FSC 0039-13.

Spectra of A, F, and G stars present low-ionization, metal lines; but any photospheric contribution to the to-

tal equivalent width in our spectra is small. The velocity offset of the absorption troughs require a non-stellar absorption component; and the MgII troughs for four of the galaxies show little or no absorption at the systemic velocity. Only the FSC 0039-13 spectrum presents absorption at $v = 0$. We attribute it to the interstellar medium in the host galaxy, likely a result of high inclination relative to our sightline.

A dominant stellar origin for the resonance absorption appears unlikely in these ULIRGs for several reasons. First, Figure 2 shows MgII and MgI equivalent widths measured from synthetic spectra, computed with the STARS2002 stellar population synthesis code (Sternberg 1998; Thornley et al. 2000; Sternberg, Pauldrach, & Hoffmann 2003; Davies et al. 2007) and the UVBLUE library of high-resolution stellar spectra (Rodríguez-Merino et al. 2005), for a broad range of star formation histories.³ Only post-starburst populations, with continua dominated by A, F, or G stars, show MgII 2796 equivalent widths of more than a couple Angstrom. The large MgII equivalent widths of FSC 0039-13, FSC 1407+05, and FSC 1630+15 are inconsistent with continuous star formation; and the other two ULIRGS do not lie near the stellar locus. Second, the ULIRG spectra lack detectable absorption from excited, electronic states of FeII, lines that are prominent in the spectra of older stellar populations in Figure 3. In addition, the synthesized spectrum of the stellar population shows MgII lines much broader than those from MgI, although smearing by the motions of stars in the galaxy could hide this difference. Previous ULIRG outflow studies estimated the stellar contamination in the NaI absorption trough from the equivalent width of the excited MgI triplet at $\sim 5200 \text{ \AA}$ (not covered by our spectra) and typically found a negligible stellar contribution (Martin 2005).

Extracting quantitative information about the absorbing material in the outflow from the absorption troughs requires a physical model. The spectra presented in this paper resolve components with intrinsic velocity widths of 100 km s^{-1} or more; and neither thermal nor turbulent motion easily explains the extremely broad, $\sim 800 \text{ km s}^{-1}$, velocity width of the absorption troughs. Macroscopic variations in velocity are required and could be associated with discrete supershells and their fragments (Fujita et al. 2009), interstellar clouds over-run by the superbubble shock (Cooper et al. 2008), eddies formed at the wind - disk interface (Heckman et al. 2000), or the velocity gradient in a smoothly accelerating wind (Murray et al. 2005). These ideas motivate descriptions with discrete velocity components, where components correspond to individual clouds or shell fragments.

In Section 3.3, we formally fit all the absorption troughs with such velocity components. For unblended, doublets, a parametric description of the absorption troughs requires fewer physical priors, however; and we apply this approach in Section 3.2 to build intuition. The key constraint throughout this modeling is the observation that many of the transitions must be optically thick, not only at the deepest part of the absorption trough but

³ All models assumed a Kroupa initial mass function from 1 to $120 M_{\odot}$, solar metallicity, and an exponentially declining star-formation rate.

at high outflow speed. To illustrate the robustness of this model-independent statement, we directly compare the absorption trough shapes among the different transitions in Section 3.1.

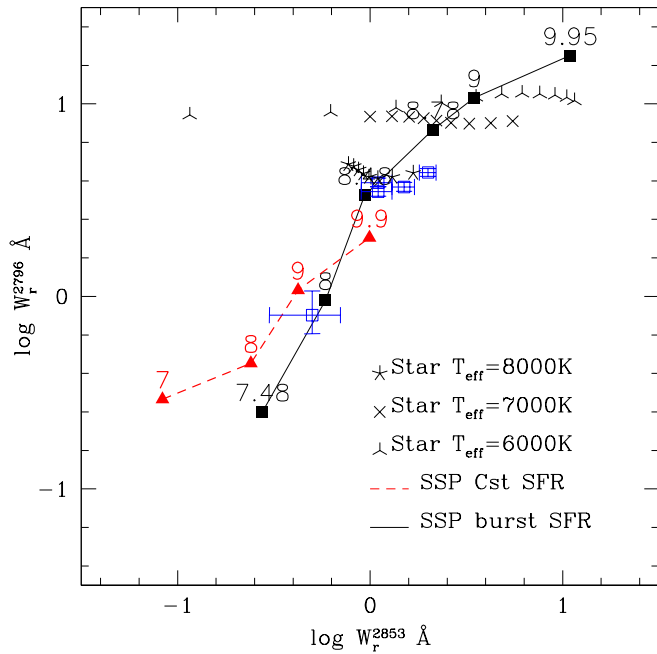


FIG. 2.— MgI and MgII absorption equivalent widths for 5 ULIRGs compared to simple stellar population models (§ 3.1) and individual stellar templates. The equivalent widths increase with increasing age, from $\log \tau(\text{yr}) = 7$ to 10, for both burst (solid squares) and continuous (solid triangles) star formation histories. In the individual stellar templates, the $\text{EW}(\text{MgII})$ is set by the effective temperature, while the $\text{EW}(\text{MgI})$ varies significantly with the gravity parameter. In § 3.1, we argue that neither the MgI nor MgII absorption equivalent widths are stellar-dominated in any of these ULIRGs.

3.1. Direct Comparison of Absorption Trough Shape in Seven Transitions

When intervening absorption is studied in quasar spectra, or the Galactic halo studied in absorption against stellar spectra, the angular size of the absorbing gas clouds exceeds that of the continuum source. Gas between the observer and the light source attenuates the continuum by an amount proportional to the logarithm of the optical depth in any transition. For a doublet, we have

$$I_B(v) = I_0 e^{-\tau_B(v)} \quad (3)$$

$$I_R(v) = I_0 e^{-\tau_R(v)}. \quad (4)$$

For interstellar conditions, the relative optical depth between electronic transitions in a single ion from the ground state, i.e. of resonance lines, is $\tau_B/\tau_R = (f_B \lambda_B)/(f_R \lambda_R)$. For the NaI and MgII doublets, the ratio of the oscillator strengths of the blue line, f_B , to the red line, f_R , is 2; and the wavelengths of the transitions are very similar. Substitution in Eqn. 3 indicates that the relative depth of the continuum-normalized absorption troughs must be $I_B(v) = I_R^2(v)$. These relations hold provided the clouds completely cover the con-

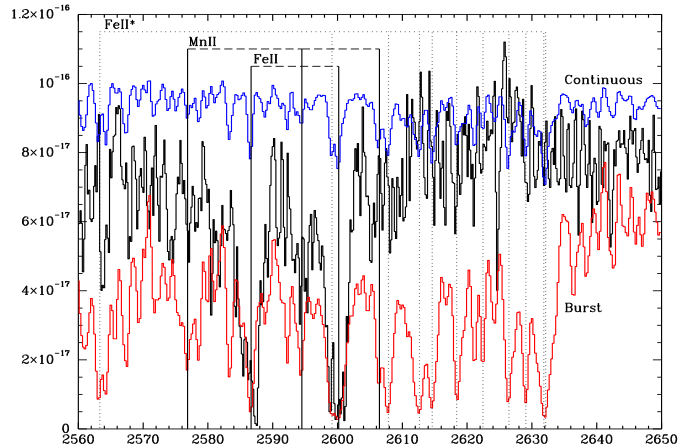


FIG. 3.— Unreddened STARS2002/UVBLUE models for a 1 Gyr old stellar population of solar metallicity vs. the FSC 0039-13 spectrum (in black) around FeII. The data show very strong FeII lines. The weaker MnII 2576.877, 2594.499, and 2606.462 lines are expected to have equivalent width ratios of 1.8:1.4:1.0, respectively. Since the upper limit on the MnII 2606 strength is low, the observed FeII 2600 trough cannot have a significant contribution from an MnII 2594 line. The spectral quality allows only upper limits to be placed on the strength of the excited FeII * lines. Excited FeII * lines are prominent in the burst model and present but weaker than our detection limit in the continuous star formation model. Models were normalized to the data at 3000Å. Modest reddening of the continuous star formation model, e.g. $A_V = 0.5$, provides a reasonable estimate of the continuum level in the FSC 0039-13 spectrum. Burst models with ages greater than 100 Myr are intrinsically too red to describe the observed continuum slope.

tinuum source over a velocity range comparable to (or greater than) the spectral resolution. In practice, when transitions with different f values saturate, both troughs appear black in noisy spectra.

Observations of NaI absorption troughs in ULIRGs cannot directly measure the relative intensities $I_B(v)$ to $I_R(v)$ due to the blending of the two absorption troughs. Previous modeling of the combined trough strongly suggests, however, that the assumption of complete continuum coverage is not met (Martin 2005,2006; Rupke et al. 2005a,b).

3.1.1. Description of MgII Absorption Troughs

The MgII absorption troughs delineate the outflow kinematics most cleanly. In FSC0039-13, the majority of the trough equivalent width is blueshifted, but the minimum intensity of the trough lies near the systemic velocity. The intensity minima are blueshifted several hundred km s^{-1} in the other MgII spectra with little or no absorption at the systemic velocity. In FSC1630+15 and FSC2349+24, the minima in the absorption troughs lie at $v \sim -400 \text{ km s}^{-1}$. The FSC1407+05 spectrum presents a broad trough from -200 to -500 km s^{-1} . The MgII 2796 and 2803 absorption troughs blend together in the FSC1009+47 spectrum, possibly due solely to the lower SNR of this spectrum. The MgII absorption troughs have residual intensities $< 10\%$ in FSC0039-12 and FSC1630+15 at minimum intensity. The residual intensity at line center is low but not zero in the other three spectra. The MgII absorption troughs are noticeably deeper than the MgI or NaI absorption troughs.

We can test the condition represented by Equa-

tions 3 and 4 by comparing the MgII $\lambda 2796$ and $\lambda 2803$ troughs in our spectra of FSC0039-13, FSC1407+05, FSC1630+15, and FSC2349+24, only FSC 1009+47 presents severe blending of the absorption components in Figure 1. Comparison of the MgII 2796 and 2803 trough shapes illustrates their nearly identical intensity at most velocities. The most significant differences appear in the FSC2349+24 and FSC1407+05 spectra where MgII $\lambda 2796$ emission fills in part of the $\lambda 2803$ trough. The assumption of unity covering factor implicit to the apparent optical depth method clearly fails. As seen in projection on the sky against the spatially extended galactic continuum, the low-ionization outflow does not uniformly cover the source.

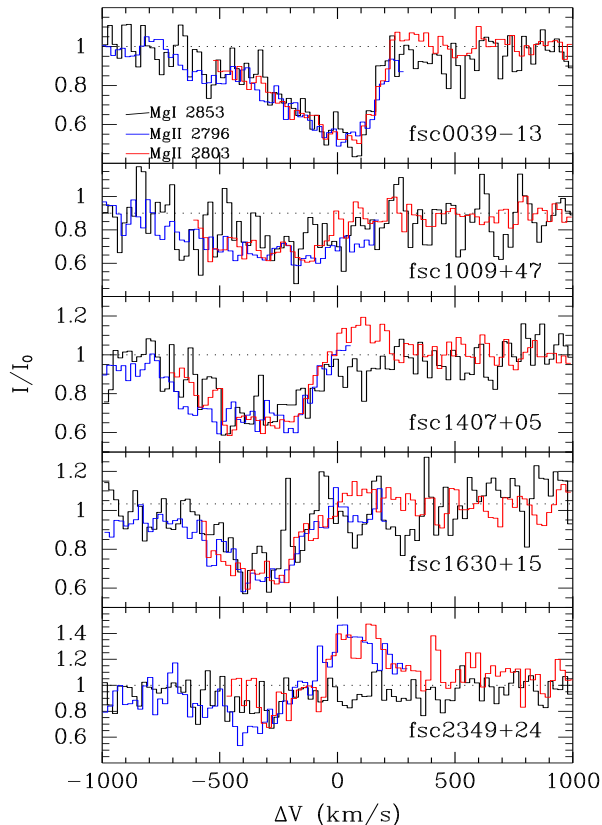


FIG. 4.— MgI with scaled MgII profiles are overlaid. To facilitate comparison the depth of the corresponding MgII absorption troughs have been reduced by factors of 2.0, 2.5, 2.0, 2.0, and 1.0, respectively. The shape of the MgII and MgI absorption troughs are indistinguishable aside from the contribution of the MgII emission.

3.1.2. Relative Shape of MgI and MgII Absorption Troughs

In Figure 4, we scale the depth of each MgII absorption trough to facilitate comparison to the shape of the MgI absorption trough. Based on our inspection of the data, we argue that the MgII and MgI absorption troughs trace gas with the same kinematics.

FSC0039-13:— We reduced the depth of the MgII absorption trough by a factor of two by multiplying $I_c(\lambda) - I(\lambda)$ by a factor 0.5 and adding the

result to the normalized continuum, $I_c(\lambda)$. The absorption troughs in MgII 2796, 2803 and MgI 2853 are essentially indistinguishable after this scaling. The MgII absorption towards FSC0039-13 is detected at velocities $\sim 100 \text{ km s}^{-1}$ higher than the maximum velocities detected in MgI. The SNR in the MgI profile blueward of -600 km s^{-1} is inadequate to definitively detect the weak absorption expected based on the shape of the MgII 2796 profile, so the MgI observation is consistent with the presence of neutral Mg up to the same outflow velocity detected in MgII.

FSC1009+47:— The scaled MgII 2796 and 2803 absorption trough is identical to that of MgI blueward of -100 km s^{-1} out to -600 km s^{-1} , where MgII 2803 blends with the red part of 2796. The high-velocity 2803 absorption makes the 2796 trough appear to be deeper than the 2803 trough between -100 km s^{-1} and $+150 \text{ km s}^{-1}$. The 2796 trough is detected to -780 km s^{-1} . The MgI trough is cleanly detected to -450 km s^{-1} ; but comparison to MgII 2803 suggests MgI is plausibly present in the outflow to at least -700 km s^{-1} . After the depth of the MgII profile is reduced by a factor of 2.5, the MgI profile is indistinguishable from the 2796 profile at high velocity and the 2803 profile at low velocity.

FSC1407+05:— The MgI and MgII 2796 lines in FSC1407+05 are both detected to velocities reaching -750 km s^{-1} . The MgII 2803 profile presents emission from 0 to $+250 \text{ km s}^{-1}$. The MgII 2796 emission is diluted by the MgII 2803 absorption at the same wavelength. The addition of the 2796 emission to the MgII 2803 absorption trough elevates the latter between velocities -750 and -500 km s^{-1} . At intermediate velocities less affected by blending, -500 to 0 km s^{-1} , the MgII and MgI profiles lie right on top of each other after reducing the depth of the MgII troughs by a factor of 2.0.

FSC1630+15:— In FSC1630+15, the shape of the MgII and MgI profiles are the same from 0 to -620 km s^{-1} after scaling MgII by a factor of 2.0. Maximum absorption is offset to -400 km s^{-1} . The MgII 2796 absorption trough is detected to -825 km s^{-1} . The SNR in MgI near these velocities is not adequate to detect the scaled MgII profile, so the velocity ranges of absorption MgI and MgII are consistent with being the same.

FSC2349+24:— The FSC2349+24 spectrum shows strong MgII emission. The 2796 emission fills in the bluest portion of the 2803 line profile. The 2796 trough reaches -650 km s^{-1} . We compare the MgII trough to MgI without any scaling. The SNR is not adequate to detect the MgI trough at outflow speeds greater than -500 km s^{-1} .

3.1.3. The MgI Absorption Trough as a Template for the Blended NaI Trough

Since we detect these ULIRG outflows in neutral Na, the spectral energy distribution incident on the outflow likely presents a Lyman edge. (See the quantitative discussion in §2.3 of Murray et al. 2007). Stellar spectra have large intrinsic Lyman edges, so it follows that the starburst, rather than AGN, likely determines the Na ionization of the outflow. We expect a similar situation

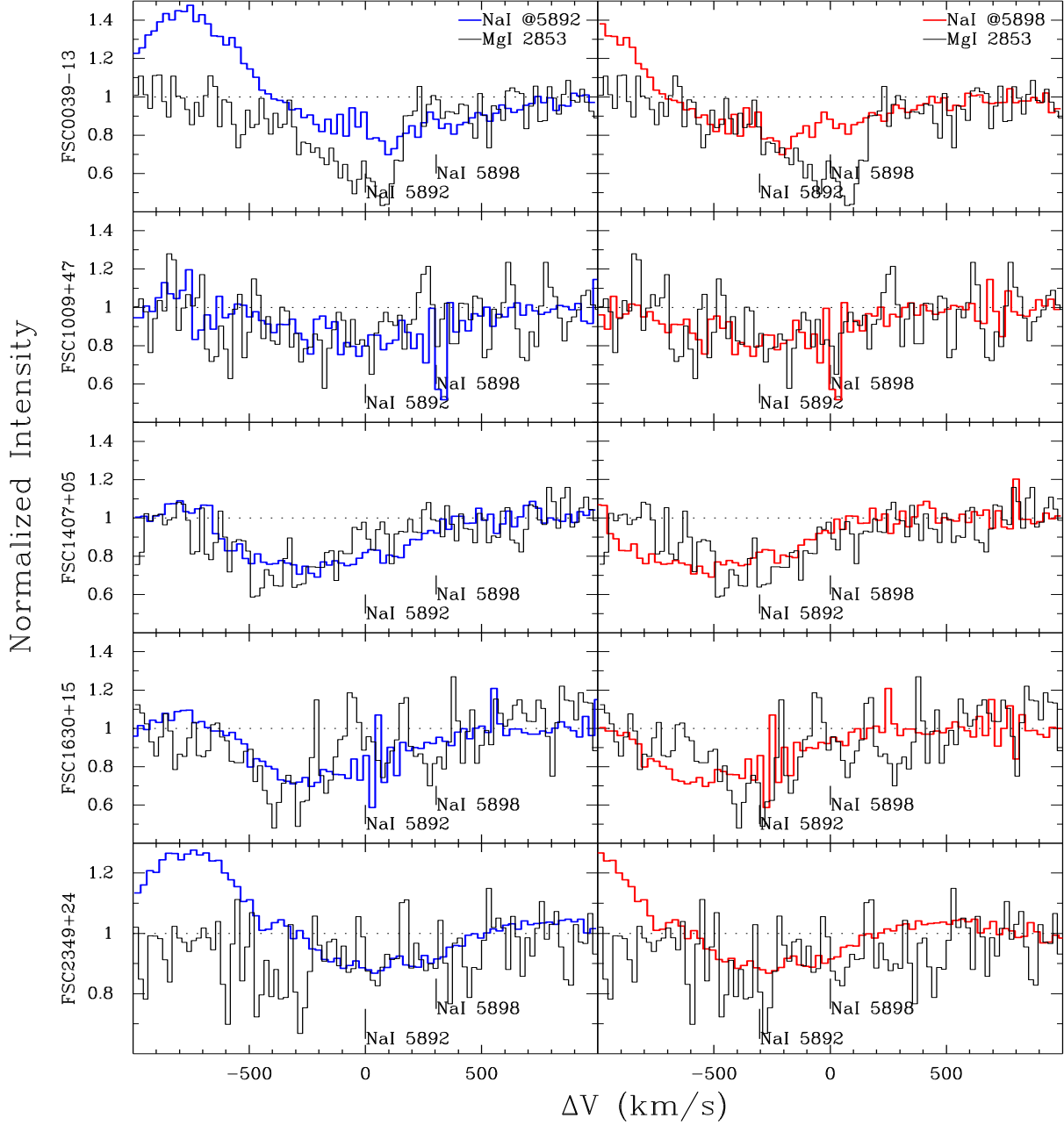


FIG. 5.— Comparison of NaI and MgI absorption line troughs in 5 ULIRGs. *Left:* The blue side of the NaI trough, dominated by the NaI 5892 transition, compared to the MgI trough. *Right:* The red side of the NaI trough, dominated by the NaI 5898 transition, compared to the MgI trough.

for *Mg*, which has an ionization potential just 2.5 eV higher than that of *Na* (7.6 eV vs. 5.1 eV). The patchy distribution of dust in ULIRGs, however, leaves open the possibility that the morphological appearance of the stellar component in the near-UV differs considerably from that at 6000Å. Absorption troughs present in these two bandpasses need not sample the same region of the outflow.

Before comparing the near-UV and optical trough shapes for the first time, it is useful to consider the relative optical depths in each transition should the absorption occur in the same clouds. Magnesium is 19 times more abundant than Na but only four times more depleted than Na.⁴ Singly ionized magnesium, MgII, is the dominant ion of Mg over a large range of density and temperature. In contrast, the Murray et al. (2007) ionization models predict a larger variation in $\chi(\text{NaI})$ from object to object, allowing a wide range of possibilities for the relative optical depth of MgI and NaI. For comparable Mg and Na ionization fractions, i.e. $\chi(\text{NaI}) \approx \chi(\text{MgII})$ where $\chi(X^{+n}) \equiv N(X^{+n})/N(X)$, the NaI 5892 optical depth and that of the weaker NaI 5898 line will be lower than the MgI 2853 optical depth.

The blending of the NaI 5892, 98 lines complicates the direct, model-independent comparison. In Figure 5, we use the MgI profile as a template for both the NaI 5892 (left column) and 5898 (right column) absorption troughs. In three of the ULIRGs, the depth of the NaI and MgI absorption troughs are similar at minimum intensity. The two ULIRG spectra with strong HeI 5877 emission present shallower troughs in NaI relative to MgI, which we explain in part by emission filling of the NaI troughs. We take account of the HeI 5877 emission filling in Section 3.3 and estimate comparable maximum outflow speeds in NaI, MgI, and MgII. Surprisingly, the modeling in Section 3.3 demonstrates that the kinematics of the NaI absorbing gas are not distinguishable from that in the low-ionization UV transitions.

FSC0039-13:— In the FSC 0039-13 spectrum, we detect NaI absorption up to -320 km s^{-1} . Emission filling from He I plausibly explains why the MgI and MgII absorption troughs extend to higher velocity. The MgI trough is nearly twice as deep as the bluer portion of the NaI trough (left panel) and three times deeper than the redder portion of the NaI trough (right panel). The HeI emission contributes to the shallowness of the blue half of the NaI trough (relative to MgI), but emission filling fails to explain the low intensity of the red half of the NaI trough over 1000 km s^{-1} from the HeI line. The deepest part of the MgI profile at $+90 \text{ km s}^{-1}$ matches the minimum in the NaI trough. At the wavelength corresponding to the same Doppler shift in the NaI 5892 transition, we find another local minimum in the blended, absorption trough. We postpone discussion of the relative intensities of the NaI 5892 and 5898 absorption troughs to Section 3.3 because both transitions contribute to the absorption at minimum intensity.

FSC1009+47:— In the FSC1009+47 spectrum, the NaI absorption trough extends from roughly the systemic velocity to about -450 km s^{-1} . At the coarse level

of comparison allowed by the poor spectral SNR, the shapes of NaI 5892 and MgI profiles match without any scaling. Better SNR at MgII shows the outflow reaches -800 km s^{-1} .

FSC1407+05:— The NaI absorption is detected to -650 km s^{-1} , close to (within one resolution element of) the maximum absorption velocity detected in MgI and MgII. The NaI and MgI absorption trough shapes are very similar, with the latter being slightly deeper.

FSC1630+15:— In FSC1630+15, the MgI profile provides a good description of the NaI absorption trough with no scaling of the NaI 5892 or 5898 lines. Absorption is detected in both troughs to -600 km s^{-1} . The SNR's of the NaI and MgI spectra do not allow detection up to the maximum velocity detected in MgII.

FSC2349+24:— In FSC2349+24, HeI emission fills part the blue-end, $v < -250 \text{ km s}^{-1}$, of the NaI absorption trough. The MgI and NaI troughs have similar intensity at other velocities.

3.1.4. Relative Strength of the FeII and MgII Absorption Troughs

The oscillator strength of FeII 2600 is about 3.5 times higher than that of FeII 2587. The similar shape of the two blueshifted FeII troughs requires even the FeII 2587 transition to be optically thick at the highest velocities measured in the outflow. Iron has only a slightly lower cosmic abundance than Mg. Using cosmic abundance ratios, the optical depth of FeII 2600 will be 57% that of MgII 2803 for comparable depletion and ionization corrections. We directly compared the shape of the FeII 2600, FeII 2587, MgII 2796, and MgII 2803 absorption troughs below, omitting the two objects with low SNR near FeII. We find similar intensity in all four troughs at comparable velocity. Section 3.3 presents quantitative, but model dependent, fits.

FSC0039-13:— From -600 km s^{-1} to $+200 \text{ km s}^{-1}$, $I_B \approx I_R$ for the FeII 2587, 2600 troughs. The FeII 2587 trough does not present the dip seen in FeII 2600 from -800 to -600 km s^{-1} . We do not detect the MnII 2576 line, so absorption from the weaker MnII 2594 transition does not produce the blue dip in FeII 2600. We also exclude blending with excited, photospheric lines based on the location of such lines in the stellar spectra shown in Figure 3. We attribute the discrepancies in the FeII profile shape over a small velocity range to a combination of statistical and systematic errors in the data, where continuum fitting uncertainties dominate the systematic error in this spectral region. The FeII 2600 trough is identical to the MgII trough (to within the error bars) over the velocity range from -600 km s^{-1} to $+400 \text{ km s}^{-1}$. The FeII 2587 trough varies in lock step with the MgII trough from -900 km s^{-1} to $+200 \text{ km s}^{-1}$. We conclude that the FeII and MgII absorption troughs sample gas with similar kinematics.

FSC1009+47:— The MgII profile for FSC1009+47 provides a good description of the blue wing of the FeII 2600 trough with no scaling. The FeII 2587 trough is slightly shallower.

⁴ Depletion quoted for cool interstellar medium of the Galaxy (Savage & Sembach 1996).

FSC1407+05.— The blueshifted wing of the *FSC1407+05* FeII spectra at $v < -200$ km s⁻¹ shares the shape of the MgII profile, but the FeII troughs are slightly shallower (amplitude reduced by 1.3 in 2600 and 1.6 in 2587). Both FeII troughs lie well below the MgII troughs from -100 km s⁻¹ to +100 km s⁻¹. The MgII 2803 profile presents a weak, but significant, emission bump from 0 to +200 km s⁻¹. No FeII emission is detected, so the FeII absorption troughs will look broader than the MgII troughs. The MgII absorption trough may share the kinematics of the low-velocity FeII trough but be filled in by emission.

3.2. Parametric Descriptions of the Absorption Troughs

In the spectral regions where the MgII 2796, 2803 absorption troughs can be directly compared, their intensities are nearly equal, $I_B \approx I_R$. Since the galaxy (continuum) likely subtends a large angle relative to that of an individual shell fragment or cloud, we might expect variation in the properties of the absorbing material as a function of the spatial and/or velocity coordinates in the outflow. A number of methods have been developed to parameterize the relative geometry of the outflow and continuum source. We apply the most common method to the absorption troughs from *FSC0039-13* and *FSC1630+15*, which show no sign of emission filling and little blending of the $\lambda 2796$ and $\lambda 2803$ lines. We then explain why two other parameterizations fail to describe the distribution of outflowing gas.

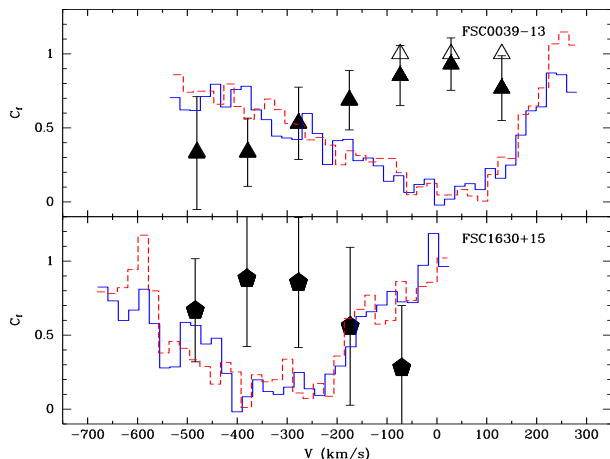


FIG. 6.— Covering fraction vs. MgII velocity. We binned to the spectral resolution and computed $C_f(v)$ from Equations 7. For *FSC0039-13*, the open symbols show the effect of removing a symmetric, zero-velocity component. For reference, the solid (blue) line and dashed (red) line show the $\lambda 2796$ and $\lambda 2803$ MgII absorption troughs. We find that the covering fraction largely determines the shape of the absorption trough. The troughs are deeper at velocities where low-ionization gas covers a higher fraction of the continuum.

3.2.1. Pure Partial-Covering Model

An approach used extensively for quasar winds (Arav et al. 2001; Arav et al. 2005; Arav et al. 2008) is to assume that a fraction $1 - C_f(v)$ of the area of the continuum source is free of absorption at velocity v ; and the optical

depth distribution in front of the covered part of the source is constant. For this parameterization, the line intensities are given by

$$I_R(v)/I_0 = 1 - C_f(v) + C_f e^{-\tau(v)} \quad (5)$$

$$I_B(v)/I_0 = 1 - C_f(v) + C_f e^{-2\tau(v)}, \quad (6)$$

where $\tau(v)$ is the optical depth at velocity v in the weaker line, here MgII $\lambda 2803$. The coefficient in the argument of the exponential in Eqn. 6 depends on the relative oscillator strengths and wavelengths of the doublet transitions. We binned the blue and red profiles to the spectral resolution; and then computed the covering fraction

$$C(v) = \frac{I_R^2 - 2I_R + 1}{I_B - 2I_R + 1}, \quad (7)$$

where the continuum has been normalized to unity, $I_0 = 1$. At velocities where measurement errors produced unphysical line intensities, $I_R < I_B$ or $I_R^2 > I_B$, we set the covering fraction to $C(v) = 1 - I_R(v)$ or $C(v) = 1.0$, respectively. By substitution, the optical depth is

$$\tau(v) = \ln \left(\frac{C(v)}{I_R(v) + C(v) - 1} \right). \quad (8)$$

Where statistical fluctuations result in $I_R < I_B$, measurement of the optical depth is not constrained. At velocities where $I_R \approx I_B$, both transitions must be optically thick; and this method cannot discriminate an optical depth of 3 from 30 in galaxy spectra of typical quality. The limited spectral resolution and low SNR of these data leave open the possibility of substantial systematic errors in our best estimate $\tau(v)$. We will refer to this method as the pure partial covering scenario with velocity-dependent covering fraction.

Figure 6 shows the covering fraction of low-ionization absorption derived this way varies significantly across the trough. Our analysis necessarily neglects components narrower than 100 km s⁻¹, which may contribute to the total gas column but are unconstrained by our spectra. The covering fraction is near unity only where the trough is black. In the *FSC0039-13* spectrum, this maximum coverage is near the systemic velocity regardless of whether we remove a symmetric, zero-velocity absorption component before computing $C(v)$. In *FSC1630+15*, the velocity of the low-ionization gas with the highest covering fraction is between 300 and 400 km s⁻¹. The covering fraction falls steadily with increasing outflow speed in *FSC0039-13*, reaching 35% at 500 km s⁻¹. Similarly, away from the velocity where the absorption trough presents minimum intensity, $C_f(v)$ declines in *FSC1630+15*. The residual intensity correlates with the derived covering fraction. We conclude that the shape of the absorption trough, $I(v)$, is strongly influenced by the velocity dependence of the covering fraction of low-ionization gas in the outflow.

Figure 7 compares the MgII $\lambda 2803$ optical depth, $\tau(v)$, to $C_f(v)$. The low-ionization gas at velocity $v \sim -600$ km s⁻¹ is apparently optically thick in the MgII transitions. At higher speeds, the blending of the blue wing of the MgII 2803 trough with the MgII 2796 line prevents a unique comparison of $I_R(v)$ to $I_B(v)$. The

solution to Eqn. 8 for for FSC0039-13 and FSC1630+15 indicates that $\tau(v)$ increases by a factor of ~ 2 and 1.5 , respectively, as the covering fraction grows by a similar factor. Such a trend is physically plausible, even probable, but is not required by the data. The method only returns a lower limit on optical depth, $\tau \gtrsim 3$. In our spectra, optical depths of 3, 30, and 300 yield essentially identical line profiles; in contrast, damping wings (not seen) would distinguish $\tau \gtrsim 10^4$. The lower limits on the optical depth, $\tau(v)$, determines the lower limit on the ionic column density in the outflow at a given velocity. Applying Eqn. 1 from Arav et al. (2001) to the optical depth in the MgII $\lambda 2803$ transition,

$$N[\text{cm}^{-2}] = \frac{3.7679 \times 10^{14}}{\lambda_0[\text{\AA}]f} \int \tau(v) dv, \quad (9)$$

we estimate total ionic column densities of $N(\text{MgII}) > 6.4 \times 10^{14} \text{ cm}^{-2}$ and $> 4.28 \times 10^{14} \text{ cm}^{-2}$ toward FSC0039-13 and FSC1630+15, respectively.

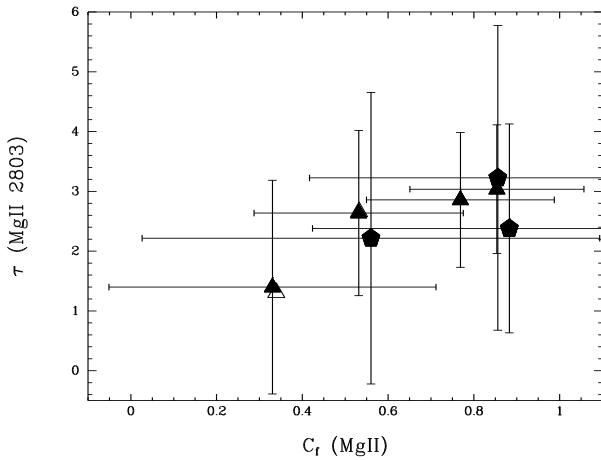


FIG. 7.— Optical depth of the MgII $\lambda 2803$ line vs. MgII covering fraction. We binned the MgII absorption troughs to the spectral resolution and then computed $C_f(v)$ and $\tau(v)$ from Equations 7 and 8. Triangles and pentagons represent FSC0039-13 and FSC1630+15, respectively. Where statistical errors led to unphysical intensity ratios, $I_B > I_R$, no upper bound on the optical depth could be obtained; and no results are shown. Removal of a symmetric, zero-velocity component in FSC0039-13 assigns zero covering fraction and optical depth to the outflow near the systemic velocity; but the fit to the outflow portion of the trough barely changes (open symbols). The data allow, but do not require, regions of the absorption trough with higher covering fraction to have higher optical depth.

3.2.2. Inhomogeneous Absorption

The pure partial covering scenario with velocity-dependent covering fraction is just one particular two-parameter (C_f, τ) description of the relative intensities of the doublet troughs. With just two absorption troughs to fit, other two-parameter models would also exactly fit the data. A real test of the model requires spectra covering additional transitions from the same ion, which is not possible with our data. We can, however, calculate parameter values for other models and examine how they change our view of the distribution of low-ionization gas in the outflow.

One such model is inhomogeneous absorption across the source. This is appealing for AGN outflows because sharp edges in the spatial distribution of absorbing gas appear unrealistic because the gas lies at distances thousands of times greater than the size of the AGN emission source (de Kool et al. 2002). Arav et al. (2005) present a simple model, where the optical depth distribution across a uniform surface brightness source varies as $\tau(v, x) = \tau_0(v)x^a$, where x describes the location (in the plane of the sky) across the projected area of the source; and x is confined to the range $[0,1]$. To produce similar intensities in the MgII $\lambda 2796$ and $\lambda 2803$ lines, they require the function $\tau(x)$ be steep, e.g. $a \gtrsim 8$. A high value of the exponent works because it yields a factor of two change in the optical depth over a relatively small number of spatial elements, x , resulting in $I(2\tau) \approx I(\tau)$. For even moderately large values of τ_0 , the optical depth will be low over at least a few tenths of the source area, and the absorption troughs will not be black.

In the ULIRG outflows, $I_R \approx I_B$ over a wide velocity range; but the MgII troughs are nearly black over a smaller velocity range. The inhomogeneous absorber model requires unphysically large optical depths to reproduce these MgII absorption troughs. Starburst outflows also do not present the problem with pure-partial covering as do AGN outflows. The rotation observed across some low-ionization outflows suggest the outflowing gas lies within a few kpc of the galaxy (Martin 2006). Hence, we find no reason to adopt an inhomogeneous-absorption model for ULIRG outflows.

3.3. Fitting Velocity Components to the Absorption Troughs

The direct method of the previous section cannot be applied to the absorption troughs in which the doublet transitions blend together and/or the absorption trough blends with one or more emission lines. A quantitative description of these absorption troughs requires fitting the parameters of functions describing each spectral component.

A covering fraction, Doppler parameter, optical depth at line center, and Doppler shift describe the attenuation of the continuum by one component, or cloud, at every wavelength, $I_j(\lambda)/I_0 = 1 - C_j + C_j e^{-\tau_j(\lambda)}$. When the absorption trough is a blended doublet, the optical depth at a given wavelength may include significant contributions from each transition, and we add the doublet optical depths at that wavelength. At any particular velocity, the two transitions of the doublet must have the same C_f , b , and Doppler shift; and atomic physics fixes the ratio of their optical depths. At the systemic velocity of the HeI 5877 and MgII emission lines, we fitted the amplitude of Gaussian intensity profile with velocity width matched to that measured for H α .

The relative intensities of the MgII and FeII doublet troughs constrain these transitions to be optically thick, setting a firm lower limit on the optical depth, $\tau_0 \gtrsim 3$, at line center. The blue skew of the absorption troughs requires at least two velocity components. When we fitted such models, however, we found a number of parameter degeneracies. We could describe the velocity width of each trough by adding additional velocity components, increasing the Doppler parameter, or further increasing the optical depth of individual components. For exam-

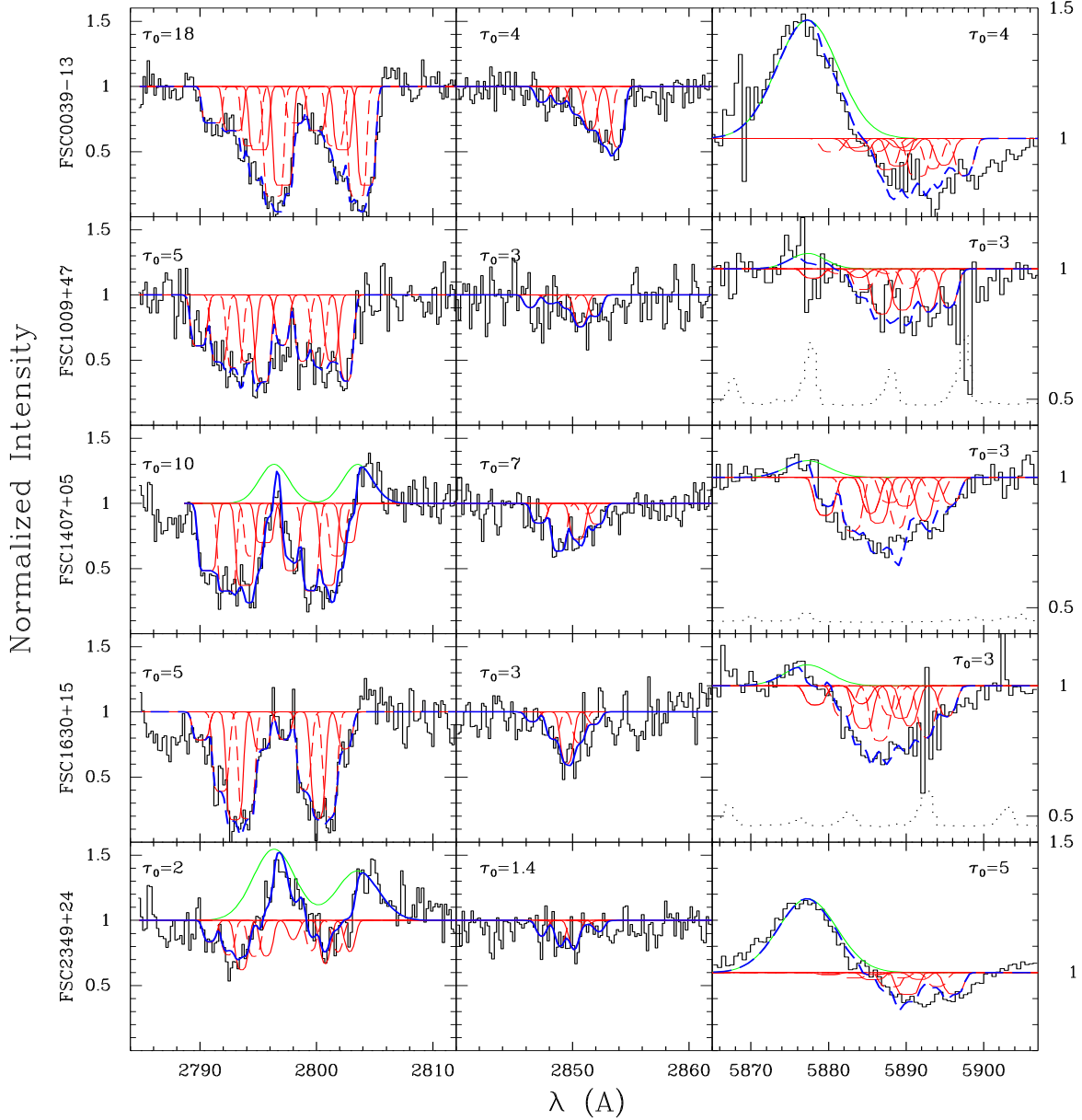


FIG. 8.— Fitted covering fraction of absorbing gas in each velocity component (red) and, when required, emission lines (green). *Left Column:* Fitted MgII absorption troughs. All velocity components have the Doppler parameter fixed at $b = 50 \text{ km s}^{-1}$ and an optical depth at line center of τ_0 . *Middle Column:* Velocity components fitted to the MgI absorption troughs. The Doppler shift and b of each component matches the corresponding MgII component, and we fitted the velocity-dependent covering fraction $C_f(v)$ and minimum τ_0 . *Right Column:* Velocity components fitted to blended NaI doublet trough. The Doppler shift and b value of each component matches the corresponding MgII component; we fit a velocity-dependent covering fraction $C_f(v)$ and the minimum τ_0 . Dotted line shows the relative intensity of sky emission; an additive constant of 0.4 has been applied to the normalized sky intensity for display purposes. Although the fitted models are not unique; they demonstrate that all three line profiles can be described with the same kinematic components.

ple, τ_0 can be made arbitrarily large by simply allowing the Doppler parameter b to shrink; and the product $b\tau_0$ of a component can be made smaller (or larger) by adding (or removing) additional velocity components. Previous studies (Rupke et al. 2005a; Martin 2005, 2006) chose the minimum number of velocity components required to describe the NaI absorption troughs.

Simulations of winds show that a single sightline intersects multiple shell fragments (Fujita et al. 2009). And high resolution spectra of starburst galaxies resolve some broad absorption troughs into components (Schwartz & Martin 2004). With this picture in mind, we assume a sightline intersects a number of velocity components, where these structures partially overlap spatially. To allow for the possibility that some of the sightlines within the beam intersect different structures, we adopt the partial overlap model introduced by Rupke et al. (2005a). Each of the n successive velocity components attenuates the continuum (and the preceding components) such that $I(v) = \prod_{j=1}^n I_j(v)$. A Maxwellian distribution provides a reasonable description of the atomic velocities within each velocity component, so a Gaussian function models the optical depth distribution, $\tau(\lambda) = \tau_0 e^{-(\lambda-\lambda_0)^2/(\lambda_0 b/c)^2}$, of each component. The covering fraction is constant across a given component but varies from one component to the next. The Doppler parameter, b , describes the turbulent motion along the line-of-sight in a given gas cloud. For purposes of illustration, we fix the Doppler parameter at $b \equiv 50 \text{ km s}^{-1}$ for all velocity components. For a typical minimum value of $\tau_0 \sim 3$, this choice yields a line width at half the trough depth around 100 km s^{-1} , consistent with the spectral resolution. We add velocity components until the fit statistic stops improving or a component becomes weaker than the detection limit. With this Doppler parameter, we need 6 velocity components to fit the MgII absorption trough in FSC 0039-13 and 5 velocity components for the other 4 galaxies.

Allowing τ_0 to vary among velocity components revealed no obvious trends with outflow velocity. The optical depth at the center of each component must be greater than three for the doublet transitions, but the probability distribution is very asymmetric with a significant tail reaching values ~ 50 times higher than the minimum value. (See the Monte Carlo approach described by Sato et al. (2009) for describing uncertainties in optical depth.) We obtained an equally good fit statistic when we required a single value of τ_0 describe all the velocity components. This assumption of a velocity-independent optical depth is our most dubious prior, and we discuss how to improve upon it in Section 3.3.3. *We adopt this approach for the purposes of comparing the velocity-dependence of the gas covering fraction among objects and among transitions. For optically-thick velocity components, the exact value of $\tau_0(v)$ has little effect on $C_f(v)$. Our approach assumes the velocity-dependence of the covering fraction determines the trough shape.*

We first fit $C_f(v)$ and the minimum value of the optical depth to the MgII absorption troughs. We found that the same kinematic components described the FeII and MgI absorption troughs well. In Section 3.3.1, we show that the minimum optical depth in the weak lines raises our best estimate of the minimum optical depth in MgII .

We test the hypothesis these velocity components also describe the blended, NaI absorption troughs and compare covering fractions among species. Table 3 summarizes the fitted parameters. Figure 8 shows the resulting fits for MgII , MgI , and NaI . We plot FeII separately in Figure 9.

3.3.1. Fitted Optical Depth

For MgII , we can compare the ionic column inferred from the fitted partial-overlap model to those estimated in Section 3.2.1. With $b \equiv 50 \text{ km s}^{-1}$, we construct the same ionic columns by setting $\tau_0(\text{MgII } 2803) = 2.75$, which implies an integrated optical depth across each velocity component of $\tau = \sqrt{\pi} c^{-1} \tau_0 b \lambda_0 = 2.3 \text{ \AA}$. The implied column densities,

$$N[\text{cm}^{-2}] = \frac{1.13 \times 10^{20} \tau_{tot}[\text{\AA}]}{\lambda_o[\text{\AA}]^2 f}, \quad (10)$$

add up to $N(\text{MgII}) = 6.4 \times 10^{14} \text{ cm}^{-2}$ for the 6 components describing FSC 0039-13. This model has the minimum τ_0 that comes close to describing the MgII absorption trough given our prior on b . The reduced chi-squared statistic improves significantly, from 1.425 to 1.143, when τ_0 is increased to 5. The fit statistic does not get much better as τ_0 is increased up to ~ 50 , so we consider $\tau_0 \approx 5$ to be our lower limit when the MgII absorption is considered independently. The pure partial-covering method also provided only a lower bound on $\tau_0(\text{MgII})$ due to saturation and low spectral SNR.

Based on inspection of the FeII absorption troughs, we argue that the actual MgII 2803 optical depths are 2 to 3 times larger than the minimum required to fit the doublet. For a cosmic abundance ratio of gas-phase iron to magnesium, the optical depth in the stronger iron line is $\tau_0(\text{FeII } 2600) \sim 0.57 \tau_0(\text{MgII } 2803) \chi(\text{FeII}) / \chi(\text{MgII})$.⁵ For the weaker FeII line, $\tau_0(\text{FeII } 2587)$ will always be 3.5 times lower than $\tau_0(\text{FeII } 2600)$. It follows that $\tau_0(\text{FeII } 2587)$ will be slightly less than unity if $\tau_0(\text{MgII } 2803) = 5$ and if our estimate for the relative ionization correction, $\chi(\text{FeII}) \approx \chi(\text{MgII})$, is correct. This model predicts the FeII (2587) absorption trough is much shallower than the FeII (2600) trough as illustrated for FSC 0039-13 and FSC 1630+15 in panels a and e, respectively, of Figure 9.

For FSC 0039-13, this model spectrum is inconsistent with the shallow FeII (2587) trough, which requires $\tau_0(\text{FeII } 2587) \sim 3$ or larger. As addressed further in Section 3.4, a difference this large in ionization fraction is unlikely given predictions from photoionization modeling. We conclude that the actual central optical depth in MgII 2803 is closer to 18 (than 5). Panel d of Figure 9 shows that the resulting MgII fit is really indistinguishable from that presented in panel b. We find the fit to FeII 2587 in panel c preferable to that in panel a.

⁵ Although Fe and Mg have similar 1st and 2nd ionization potentials, the ionization equilibrium is complicated by the larger role of dielectronic recombinations for Fe (Shull & Van Steenberg 1982). The Murray et al. (2007) photoionization calculation for outflows indicates that the largest difference in the MgII and FeII ionization fractions occurs at high gas density, $6 \times 10^5 \text{ cm}^{-3}$, for the softest SEDs, when $\chi(\text{FeII})$ can be twice as large as $\chi(\text{MgII})$.

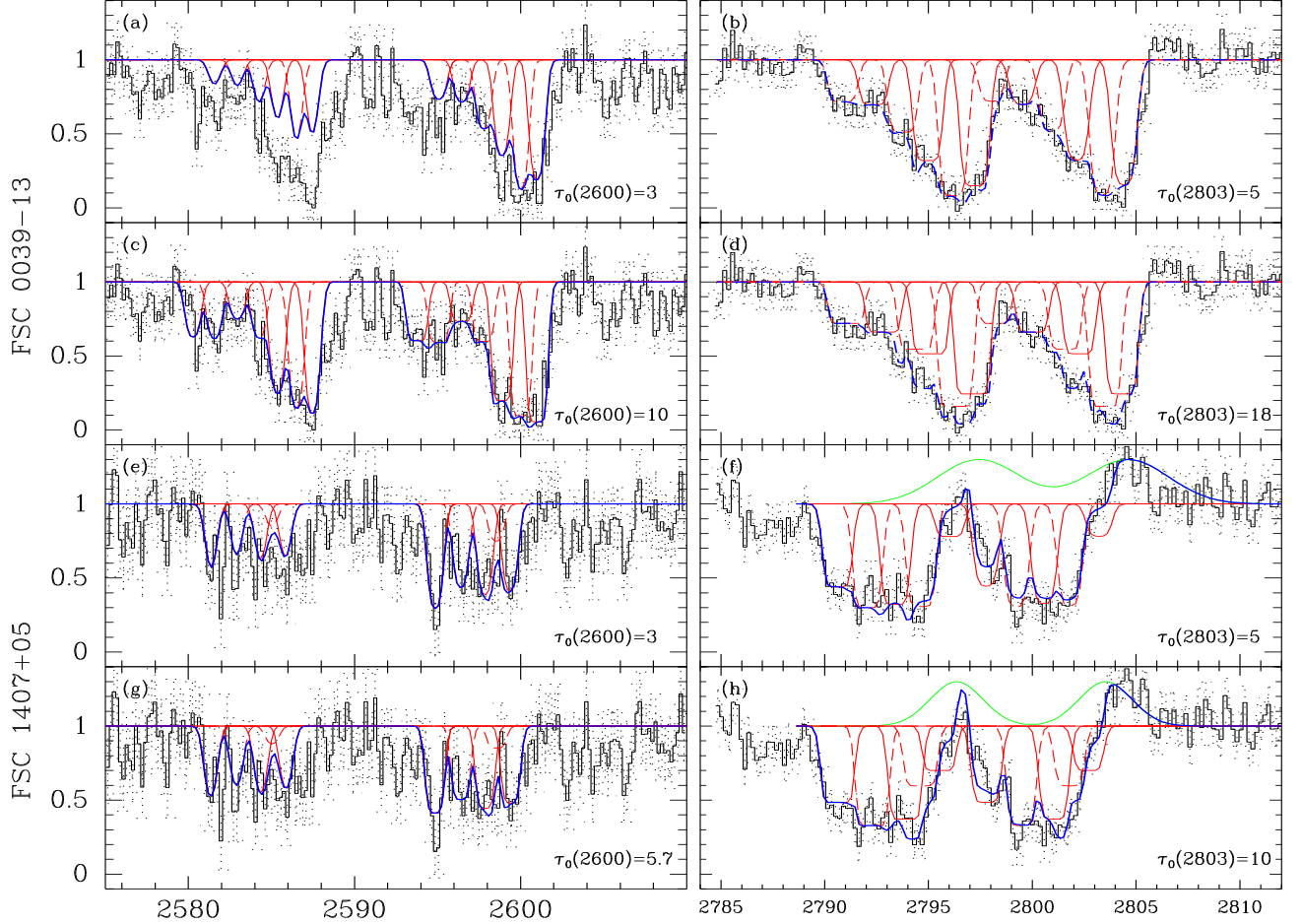


FIG. 9.— Constraints on optical depth from comparison of FeII and MgII absorption troughs. The FeII model in the left panel has $\tau_0(\text{FeII } 2600) = 0.566\tau_0(\text{MgII } 2803)$. The top and bottom two panels show FSC 0039-13 and FSC 1407+05, respectively. (a,b) *FSC 0039-13*. Assumes the minimum MgII optical depth that fits MgII 2795 and 2803, i.e. $\tau_0(\text{MgII } 2803) = 5$. With $\tau_0(\text{FeII } 2600) = 3$, the FeII 2587 lines are not nearly strong enough. (c,d) *FSC 0039-13*. Fitting the FeII 2587 trough requires $\tau_0(\text{FeII } 2600)$ of at least 10, even when a 7th velocity component is included. Increasing $\tau_0(\text{MgII } 2803)$ to 17.6 is not inconsistent with the MgII troughs. (e,f) *FSC 1407+05*. Assumes the minimum MgII optical depth that fits MgII 2795 and 2803, i.e. $\tau_0(\text{MgII } 2803) = 5$. With $\tau_0(\text{FeII } 2600) = 3$, the FeII 2587 lines are not quite strong enough. The green line shows the fitted emission component. (g,h) *FSC 1407+05*. Fitting the FeII 2587 trough requires $\tau_0(\text{FeII } 2600)$ of at least 5.7, even when a 7th velocity component is included. Increasing $\tau_0(\text{MgII } 2803)$ to 10 is not inconsistent with the MgII troughs. *These results suggest the MgII optical depth is likely a factor of ~ 2 to 3 larger than the minimum required by the data.*

For FSC 1630+15, the FeII 2587 absorption trough is slightly deeper than the prediction from the minimum $\tau_0(\text{MgII } 2803)$ model. Increasing $\tau_0(\text{MgII } 2803)$ and $\tau_0(\text{FeII } 2587)$ to 10 and 1.6 provides an acceptable fit; larger optical depths make the FeII 2587 trough deeper than observed in this case. We examined the UVBLUE spectra of synthesized stellar populations to determine if other lines might be blended with the FeII 2600 line. We identified resonance transitions from MnII, marked in Fig. 3. The MnII 2594.499 transition does not cause the depression seen at slightly shorter wavelengths because the stronger MnII 2576.877 line is not detected. The SNR around the FeII 2587, 2600 lines is not adequate for further comparison in the other objects.

Our observation of a single MgI transition does not directly constrain the MgI 2853 optical depth. The optical depth in MgI is

$$\tau_0(\text{MgI } 2853) = 6.1\tau_0(\text{MgII } 2803)\chi(\text{MgI})/\chi(\text{MgII } 2803)$$

We argued that $\tau_0(\text{MgII } 2803)$ reaches at least $\sim 10 - 18$, so the neutral Mg fraction must be less than 1 to 2 percent to produce an optically thin MgI 2853 trough. It seems more likely to us that MgI 2853 is optically thick. The covering fraction then determines the shape of the MgI absorption trough, $I(v) \approx 1 - C_f(v)$. Since covering fraction dictates both the MgI and MgII absorption trough shape, they have a similar appearance, as shown quantitatively in the middle column of Figure 8. That the MgII troughs are deeper indicates that only a fraction of the cloud volume contains much neutral Mg.

The fitted models in Figure 8 assume equivalent kinematic components for NaI and MgII. For a cosmic abundance ratio, $N(\text{Mg})/N(\text{Na}) = 19.07$, the NaI optical depth, $\tau_0(\text{NaI } 5898) = 0.115\tau_0(\text{MgII } 2803)\chi(\text{NaI})/\chi(\text{MgII } 2803)$, will be lower than that of MgII 2803 for similar ionization fraction. In Section 3.4, we argue that $\chi(\text{NaI})/\chi(\text{MgII})$ may be of order unity for soft spectral energy distributions (SED) with $L_\nu^{UV}/L_\nu^{FIR} \sim 10^{-9}$ but will vary among outflows, dropping to $\chi(\text{NaI})/\chi(\text{MgII}) = 0.001$ for hard starburst SEDs.

When the weaker NaI line is optically thin, the fitted NaI models fall well short of the observed intensity in the redder half of the absorption trough. The models shown in Figure 8 have $\tau_0(5898) = 3$ for 4 galaxies and 5 for FSC 2349+24. The ratio of these lower limits to those for $\tau_0(\text{MgII } 2803)$ in the same objects is 0.3 or more. Since the photoionization models, and consideration of depletion factors, disfavor a situation with $\chi(\text{NaI})/\chi(\text{MgII}) > 1$, the moderate optical thickness required for NaI suggests $\tau_0(\text{MgII } 2803)$ could easily be a factor ~ 2 higher than that required by $\tau_0(\text{FeII } 2587)$. As discussed in Section 3.1.1, however, the NaI and MgII absorption troughs could probe physically distinct regions of the outflow.

3.3.2. Constraints on Covering Fraction

The attraction of forcing the same kinematic components is that we can directly compare covering fraction of different species as a function of velocity, as summarized in Table 3. The fitted C_f values for the FeII velocity components come out similar to the values for MgII. The maximum covering fraction in low-ionization gas occurs at minimum intensity by construction, and we again associate the velocity of maximum covering fraction with

the speed of swept-up shells at breakout. The covering fraction decreases towards higher outflow velocity.

Independent of any particular model, the shallow troughs of MgI relative to MgII require a lower covering factor for the former at every velocity. The χ_ν^2 -fitting approach demonstrates that the shape of the MgI absorption trough can be well described by the same velocity components as the MgII troughs and further quantifies the change in covering fraction. Figure 10 compares the fitted covering fractions for MgII and MgI. The covering fraction for neutral gas remains roughly half that of the MgII at all velocities. Given the similar kinematics but constant offset in projected area, we suggest that the MgI absorption originates in denser regions of larger structures traced by MgII.

The fitted NaI covering fraction is similar to that fitted to MgI for each velocity component. Sodium and magnesium have similar first ionization potentials, 5.1 eV for Na, and 7.6 eV for Mg. In the FSC0039-13 spectrum, emission filling could explain shallow NaI 5892 trough, relative to MgI; but the emission is not broad enough to account for the shallow NaI 5898 trough. We suggested that the FSC 0039-13 sightline intersects more of the galactic, gas disk than our other observations; and the high inclination of this disk means we probe the swept-up shell where it has stalled in the disk. The extra attenuation at high inclination would likely produce larger than average differences between near-UV and optical continuum morphology. High-resolution imaging in these bands may yield further insight into why the covering fraction of neutral, alkali metals differs by almost a factor of two between the near-UV and optical sightlines. In more typical ULIRGs, the similar kinematics of NaI absorption and that of MgI, suggest the MgI velocity components and $C_f(v)$ might be applied as template for deblending the NaI absorption trough into its NaI 5892, 98 components.

3.3.3. Minimum Mass-Loss Rate

In a spherical outflow geometry, the mass flux in the low-ionization outflow, $\dot{M}_c(R) = \Omega C_f(R)v(R)\rho_c(R)R^2$. The mass column, $\bar{m}N_H(v) = \int_{R_1}^{R_2} \rho(r)dr$, measured for any velocity carries a mass flux of $\dot{M}(v_i) = \Omega\bar{m}N_H(v_i)C_f(v_i)v_iR_1R_2/(R_2 - R_1)$, where the distance and radial depth of the component are model dependent. We expect most of the mass-loading in the starburst region and therefore that $\dot{M}(r)$ be approximately constant throughout the flow. For this to happen, the product $\tau_{0,i}C_{f,i}v_i$ needs to decrease as the radial distance to component i , r_i^{-1} , increases. Our fitted values of covering fraction decline with increasing velocity, but the product $v_iC_f(v_i)$ grows with increasing outflow velocity. Obtaining a constant mass flux requires the central optical depth to decline with increasing velocity. If we choose the minimum optical depth allowed for the highest velocity component, then one can construct the values $\tau_0(v)$ from $v < \max v$ needed to raise the mass flux at lower velocities to the same outflow rate, i.e. $\dot{M}(v)$ equal to a constant. We obtain the equivalent answer by estimating the mass flux from the highest velocity component.

For FSC 0039-13, the velocity component at 571 km s⁻¹ carries a mass flux of $\dot{M} \geq$

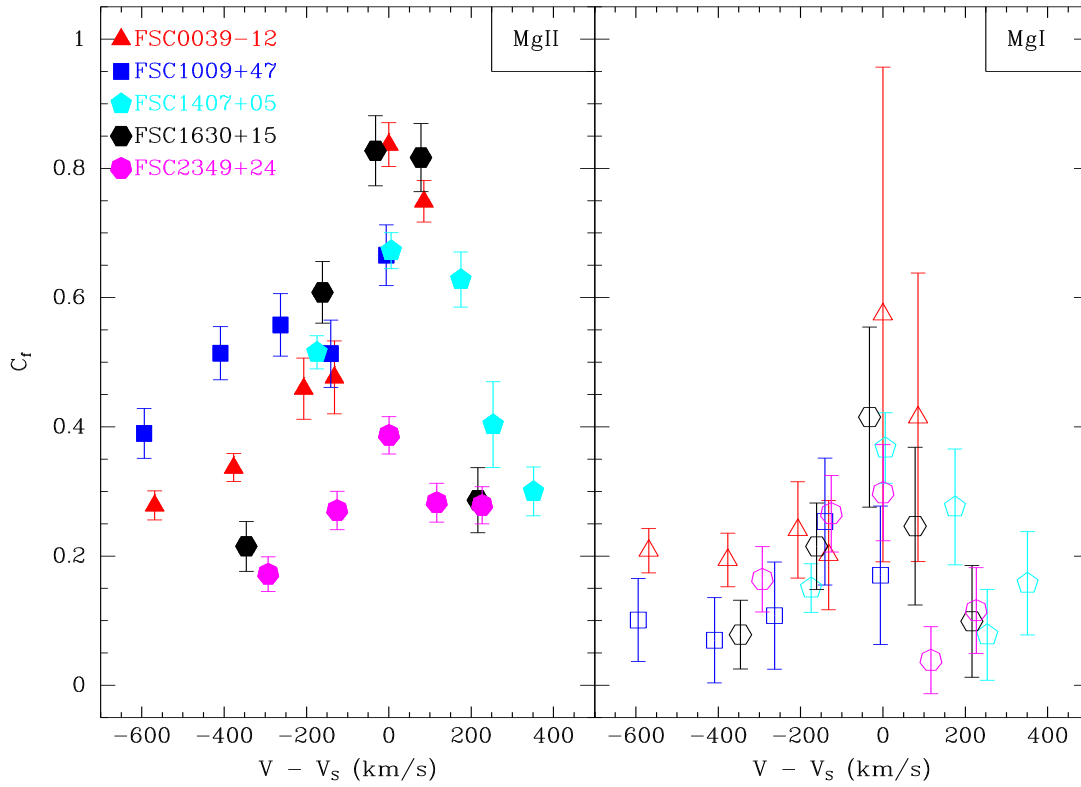


FIG. 10.— Fitted covering fractions to MgII (solid symbols) and MgI (open symbols) absorption troughs in five ULIRGs. Each component's velocity is shown relative to the velocity of the component having minimum MgII intensity; this component may be associated with the outflow velocity of a recently disrupted supershell. The shape of the absorption trough is dictated by the velocity-dependence of the covering fraction because each velocity component is optically thick. This modeling approach quantifies both the lower covering fraction of neutral Mg relative to singly-ionized Mg in the outflow and the trend towards lower covering fractions at high velocity.

$6 M_{\odot} \text{ yr}^{-1} \chi(\text{MgII})^{-1} R / \Delta R (R/10 \text{ kpc}) (\Omega/4\pi)$, where the lower limit comes directly from the requirement that $\tau_0(2587) \geq 2.7$. The velocity component at 615 km s^{-1} in the FeII absorption troughs of FSC 1407+05 requires $\dot{M} \approx 5 M_{\odot} \text{ yr}^{-1} \chi(\text{FeII})^{-1} R / \Delta R (R/10 \text{ kpc}) (\Omega/4\pi)$. In Section 3.4, we will argue that the ionization corrections for MgII and FeII are of order unity. The unknown distance to the absorbing gas and radial thickness of the component leave order-of-magnitude uncertainty in the lower limit.

Comparison of cosmic abundances and atomic data indicates $\tau_0 = 3$ will yield the highest mass-loss rate for NaI 5898, with FeII 2587 about 66% as large. To make the implied mass columns agree, the minimum optical depth in FeII 2587 would need to be $4.5 C_f(\text{NaI}) / C_f(\text{FeII}) \chi(\text{FeII}) / \chi(\text{NaI})$, or roughly $2.25 \chi(\text{FeII}) / \chi(\text{NaI})$. In Section 3.4, we find the upper bound on the correction to the minimum optical depth, $1/\chi(\text{NaI})$ could reach 10^3 for those ULIRGs with relatively hard SEDs. The lower limits on the mass fluxes likely yield an accurate picture for some systems but underestimate the true mass-flux in low-ionization gas by orders of magnitude in others.

3.4. Gas Volume Density

The volume density of the low-ionization gas varies widely among outflow models. Figures 4 and 5 of Murray et al. (2007) illustrate the sensitivity of the MgII and NaI ionization fractions to the gas density. Since the saturated lines provide only lower limits on the column densities of MgI and MgII, we cannot directly estimate the ionization fraction, thereby constraining the volume density. The null-detection of absorption from collisionally-excited levels above the ground state provides a useful upper limit on the electron density, however. The most relevant excited transitions of FeII* are marked in Figure 3; see Korista et al. (2008) for a summary. We compute this upper limit and then discuss how it constrains ionization fraction in the outflow.

Above the critical density, the level populations approach their Boltzmann ratio, and we can easily calculate the relative strengths of absorption lines from different energy levels. The lowest energy level above the ground state, $E = 385 \text{ cm}^{-1}$, has the lowest critical density. Our spectra cover the second strongest line from the multiplet with this lower energy level, FeII* 2612.6542.

In the FSC0039-13 spectrum, we expect FeII* 2612.6542 to be the strongest excited line. We place an upper limit on the observed equivalent width using the continuum SNR and assuming a line-width comparable to a spectral resolution element. The 5σ upper limit on the corresponding rest-frame equivalent width is 0.40 \AA . For comparison, we also fitted a single-absorption-line model with $b \equiv 50 \text{ km s}^{-1}$ and $C_f \equiv 1$ to the spectrum. At the systemic velocity, we find $\tau_0(\text{FeII}^* 2612) < 0.30$, a value typical of this spectral bandpass. We obtain a more conservative limit if we repeat this procedure where the largest continuum deviation occurs at -850 km s^{-1} ; and we find $\tau_0(\text{FeII}^* 2612) < 0.62$. This more conservative limit corresponds to a column density, $N(\text{FeII}^*) < 6.26 \times 10^{13} \text{ cm}^{-2}$ per component.

The optical depth in the individual velocity com-

ponents of the weakest, detected resonance line is $\tau_0(\text{FeII} 2587) \geq 3$. Each of the 6 velocity components had $b \equiv 50 \text{ km s}^{-1}$, so the lower limit on the column density in the ground state is $N(\text{FeII}) > 5.61 \times 10^{14} \text{ cm}^{-2}$. Our measurements place a solid upper limit on the relative column densities in the first-excited and ground states, $N(\text{FeII}^*) / N(\text{FeII}) < 0.11$, and likely less than 0.05. For densities well above the critical density this ratio would be ~ 0.75 with a slight dependence on temperature. Using the level population calculations from Figure 3 of Korista et al. (2008), we conservatively limit the electron density to $\log n_e < 3.5$ (or 3.4) for a temperature of $1 - 1.5 \times 10^4 \text{ K}$ (or $5 \times 10^3 \text{ K}$), respectively. The stronger limit of $N(\text{FeII}^*) / N(\text{FeII}) < 0.05$, which applies if the highest density gas is at low velocity, lowers $\log n_e$ to 3.1 (or 3.0), respectively, at $T = 1 - 1.5 \times 10^4 \text{ K}$ (or $T = 500 \text{ K}$).

The gas density is important for understanding the relationship between the hot wind and the outflow observed in UV-optical absorption lines. Photoionization equilibrium likely sets the temperature of the low-ionization gas at about 10^4 K . The density of the cool, low-ionization gas must be $> 50 \text{ cm}^{-3}$ to be in pressure equilibrium with the hot wind, where $P_h \gtrsim (10^7 \text{ K})(0.05 \text{ cm}^{-3}) \sim 5 \times 10^5 \text{ K cm}^{-3}$. Outflows accelerated by radiation pressure on dust grains do not require a hot wind at all (Murray et al. 2005), allowing the low-ionization gas to have much lower density. Our upper limit on the gas density does not challenge the multi-phase models.

Our result does eliminate the Murray et al. (2007) ionization models with $n \sim 6 \times 10^4 \text{ cm}^{-3}$ or larger (see their Figures 4 and 5). We can confidently claim that MgII is the dominant ionization state of Mg. For any reasonable starburst spectral energy distribution (SED), $\chi(\text{MgII}) \geq 0.7$; and the neutral fraction is less than 30%. The correction from the ionic columns of $N(\text{MgII})$ (and $N(\text{FeII})$) to the elemental columns will be relatively minor. This knowledge of the Mg ionization balance suggests the MgI 2853 optical depth significantly exceeds its minimum value of 3. Obtaining the same total column of Mg from the MgI 2853 and MgII 2803 components requires

$$\tau_0(2853) = 6.1 \frac{\chi(\text{MgI}) C_f(\text{MgII})}{\chi(\text{MgII}) C_f(\text{MgI})} \tau_0(2803), \quad (12)$$

or $\tau_0(2853)$ up to $5.2\tau_0(2803)$ when $\chi(\text{MgI}) = 0.3$ and $C_f(\text{MgI}) = 0.5C_f(\text{MgII})$.

Eliminating very high density rules out a high neutral fraction of Na. Interpolating between the curves in Figure 4 of Murray et al. (2007) to a density of 1000 cm^{-3} , the NaI ionization fraction plummets from unity, when $L_{UV}/L_{IR} \leq 10^{-9}$, to $\chi(\text{NaI}) \sim 10^{-3}$ when the SED hardens to $L_{UV}/L_{IR} \sim 10^{-4}$. In contrast, only at very high gas density does the neutral Mg fraction change rapidly with spectral hardness. The ionization potential of Mg is 2.5 eV higher than that of Na..

3.5. Emission

Our spectrum of FSC2349+24 very clearly shows MgII emission. The emission line appears to be a bit redshifted, but we argue that the MgII absorption attenuates the blue side of the emission profile. The only other spectrum that definitely presents MgII is FSC1407+05.

The MgII 2803 profile shows the emission from 0 to +250 km s⁻¹. The corresponding MgII 2796 line is less obvious because of MgII 2803 absorption at the same wavelength. We suggested that emission filling of the MgII trough explains the deeper absorption in the FeII trough relative to the MgII trough near systemic velocity.

Weiner et al. (2009) discovered MgII emission in a subset of $z \sim 1.4$ galaxies with outflows and argued that the composite spectrum of the non-emission galaxies presented weak emission. They demonstrated the presence of the emission by fitting the red-shifted portion of the MgII 2803 absorption trough with a symmetric absorption component at the systemic velocity. Removal of this component yielded a redshifted emission component in MgII 2796. This technique cannot be applied to four of five galaxies in our sample because their MgII absorption troughs present no absorption at $v > 0$ km s⁻¹. Removing a symmetric, zero-velocity component fitted to the redshifted absorption trough in FSC0039-13 reveals no significant emission excess in MgII 2796.

The origin of the MgII emission is not completely clear, but we adopt the hypothesis that the MgII lines are excited by recombination. The two objects presenting emission are classified as Sey 2 on the basis of their optical emission-line ratios, suggesting the ionizing spectrum is harder. The absence of extended MgII emission in the 2D spectra of FSC1407+05 and FSC2349+24 rules out a scattering origin from a galaxy-scale nebula.

The fitted profiles are shown in Figure 8. In FSC1009+47, the red side of the FeII troughs are marginally lower than those of MgII, hinting at a hidden emission component in the latter. However, inclusion of an emission component in the model for any of the other three galaxies does not improve the fit to the MgII absorption trough. In fact, any emission component at the systemic velocity significantly degrades the fit if the maximum intensity is more than 10% of the continuum level. We conclude that only two of the five ULIRGS present significant MgII emission. In contrast, an He I 5876 emission improves the model for the NaI absorption trough in all five galaxies. The line is strongest in FSC0039-13, which is the only object classified as an HII galaxy in our sample.

3.6. Dynamical Ages of Targets

In the popular “cool ULIRGs \rightarrow warm ULIRGs \rightarrow quasars” evolutionary scenario, as suggested by Sanders et al. (1988), one expects the AGN to provide the increase in bolometric luminosity. Advanced mergers in the 1 Jy sample tend to have higher luminosity (Veilleux et al. 2002). While our sample does contain rather luminous ULIRGs, their 25-60 μ m colors, see Table 1, are all red enough to be classified as cool ULIRGS, i.e. $f_{25}/f_{60} < 0.2$.

Following the morphological classification scheme outlined in Veilleux et al. (2002), the most *advanced mergers* we observed are FSC0039-13 and FSC1407+05. These are single nuclei systems with a compact morphology and little tidal structure. The dynamically younger merger, FSC1009+47, presents tidal tails but the nuclei have coalesced. The tails extend to 29 kpc in FSC1009+47 (Veilleux et al. 2002). Our second spectrum for FSC1009+47 is extracted 44 kpc south (along

the slit) of the nucleus. Veilleux et al. (2002) classify this feature as a prominent knot in a tidal arm rather than a second nucleus because it is not detected in their K' image. Pre-merger sources with separated nuclei are rare in the 1 Jy sample, but we observed at least two such objects. FSC1630+15 is a close binary, separation 4.4 kpc (Veilleux et al. 2006); and FSC2349+24 is a wide binary, separation 14.5 kpc.

Among this small sample we found no evolutionary trends in low-ionization outflow properties. We compared the outflow properties along the sightlines to each nucleus in the double systems. The outflow was always seen in each spectrum.

4. DISCUSSION

We detected outflows in 5 ULIRGs in ground-state absorption from NaI, MgI, MgII, and FeII and illustrated the remarkably similar shapes of the absorption troughs in all these transitions. We then demonstrated that the velocity-dependence of the gas covering fraction determines the trough shape. Similarities in trough shape suggest these species reside in the same, low-ionization gas structures. Because MgII (and FeII) absorption covers a higher fraction of the continuum source, at a given outflow velocity, than do neutral Mg and Na, we argue that the absorbing clouds or filaments are not homogeneous.

The Doppler shift of the absorbing gas does not identify its position along the line-of-sight. In particular, no consensus had been reached previously as to whether the highest velocity material detected resides close to the starburst region or at much larger radii. A close connection likely exists between this neutral-atomic gas, outflowing dust, and large-scale molecular outflows. Images revealing the presence of dust and molecular gas in M82 out to a few kpc (Walter et al. 2002; Hoopes et al. 2005; Veilleux et al. 2009b) provide strong evidence for the survival (or continuous creation) of dense clouds despite ablation by the hot wind and evaporation, as described (for example) by Marcolini et al. (2005).

Along the outflow axis of M82, it remains unclear whether the denser material shares the same kinematics as the H α emission. The H α Doppler shift does increase with increasing distance along the minor axis (Heckman et al. 1990; Shopbell & Bland-Hawthorne 1998; Martin 1998), consistent with acceleration. However, we lack such well-resolved, position-velocity information for most nearby (and all high-redshift) galactic outflows. In this section, we describe what the velocity-dependence of the gas covering fraction may imply about the location of the low-ionization absorbing gas along the line-of-sight. We begin by considering some pedantic dynamical models, starting with the blowout of a superbubble as described by DeYoung & Heckman (1994).

4.1. Development of a Galactic Wind

The thermalized energy from supernova explosions drives a shock front through a galaxy, sweeping interstellar gas into a thin, radiating supershell (Tenorio-Tagle & Bodenheimer 1988; Shull 1993). While the growing shell remains smaller than the pressure scale height of the interstellar medium, it plows through an ambient medium of essentially uniform density; and the shell decelerates with velocity falling as $v \propto t^{-2/5}$, or equiva-

lently $v \propto R^{-2/3}$, for a continuous injection of mechanical energy (Weaver et al. 1977). The shell mass grows linearly with the bubble volume at this stage, and the mass column through the shell grows linearly with radius

$$\bar{m}N(r) = 1/3r\rho_0, \quad (13)$$

where ρ_0 is the average density of the ISM. During the supershell phase, the covering factor of the low-ionization gas will be unity provided the shell traps the ionization front.

Emission-line images of nearby, starburst galaxies show that supershells outgrow their host galaxies. We expect the shell to accelerate when the density gradient becomes steeper than $\rho(r) \propto r^{-2}$ (McKee & Ostriker 1988), a highly unstable situation in which a dense shell pushes on more rarefied gas. Numerical simulations show that the shell breaks up due to hydrodynamic instabilities at a few pressure scale heights (MacLow, McCray, & Norman 1989). The evolution of the shell fragments has received relatively little attention, but they are clearly one source of low-ionization gas that will absorb continuum emission. Additional sources of low-ionization gas include hydrodynamic instabilities induced by shear at the disk – wind interface (Heckman et al. 2000) and pre-existing, interstellar clouds over run by the supershell (Cooper et al. 2008).

A primary origin for the low-ionization outflows in shell fragments is appealing because it naturally explains the velocity offset of the MgII absorption troughs from the systemic velocity. Due to the high central concentration of gas in ULIRGs, the pressure scale-height is several times smaller than the value $h_z \sim 100$ pc typical of normal galaxies; and the blowout radius $R_0 \sim 3h_z \sim 200$ pc. By the time of blowout, the mean speed of a shell has dropped to

$$v(R) = 164 \text{ km s}^{-1} \left(\frac{L_w}{7.08 \times 10^{43} \text{ erg s}^{-1}} \right)^{1/3} \left(\frac{10^3 \text{ cm}^{-3}}{n_H} \right)^{1/3} \left(\frac{200 \text{ pc}}{R} \right)^{2/3}, \quad (14)$$

where the mass per H atom is $\bar{m} = 1.4m_H$ in the ambient medium and L_w , the rate of mechanical energy injection, has been scaled to a SFR representative of ULIRGs, i.e. $100 M_\odot \text{ yr}^{-1}$.⁶ A shell velocity $\sim 200 \text{ km s}^{-1}$ can describe the Doppler shift of the deepest part of the MgII absorption troughs in Figure 1b-1e. A sightline at high inclination (i.e. close to the plane of the gas disk) would intersect a lower velocity shell due to the higher average gas density in the plane. We appeal to this scenario as a plausible explanation for the kinematics of the MgII absorption troughs in FSC0039-13, which are deepest near the systemic velocity.

Numerical simulations of ULIRGs (e.g. Fujita et al. 2009) confirm that shell velocities decline to 200–300 km s^{-1} by the time of blowout and suggest that, following blowout, the hot interior of the bubble accelerates outward creating a hot wind with terminal velocity $v_h \approx \sqrt{3}c_s \sim 940T_7^{1/2} \text{ km s}^{-1}$. Fujita et al. did not

follow the shell fragments very far into the halo; they simply assumed the *clouds* coast outwards on ballistic trajectories. Whether or not cosmic rays (Breitschwerdt 2008; Everett et al. 2008; Socrates et al. 2008), radiation pressure, and/or the ram pressure of the hot wind further accelerates the low-ionization gas remains an important question.

Murray et al. (2005) analytically modeled low-ionization outflows accelerated by the ram pressure of a hot wind and outflows accelerated by radiation pressure. It remains challenging to observationally distinguish not only these two types of momentum-driven outflows but also the energy-conserving, ballistic trajectories. The former accelerate quickly and then coast. The latter coast for a large distance before gradually decelerating. Factors favoring radiative-driving include an empirical correlation between outflow speed and escape velocity (Martin 2005), the high dust content of ULIRGs, and the high luminosity of ULIRGs. Reasonable objections include the small number of dwarf galaxies used in the outflow speed correlation, the difficulty of coupling radiative momentum to the gas in dust-poor, lower luminosity dwarf galaxies, and evidence for the presence of hot winds in ULIRGs (Sciortino, V. & Martin, C. L. in preparation).

For purposes of illustration, we consider acceleration by the ram pressure of a hot wind following blowout. The shell radius, R_0 , and velocity, v_0 , at blowout set the initial conditions at the start of the wind phase. In a spherical outflow geometry, the ram pressure drops as the inverse-square of the radial distance, so clouds accelerate over a relatively short spatial scale. The terminal velocity of any shell fragment depends on its column density, with the low columns reaching, at most, the hot wind velocity, $v_c \approx v_h$ (Martin 2005). *The absorption troughs presented in this paper require the covering fraction of shell fragments to decrease with increasing velocity. This situation can be achieved by tuning the distribution of cloud column densities. The lowest column density fragments, which reach the highest terminal velocities, would need to be relatively rare, covering less area than higher column density clouds. Alternatively, the geometrical dilution of clouds offers a simpler way to achieve the desired result.* We demonstrate this largely geometrical effect in Section 4.2. Further numerical work, beyond the scope of this paper, will be required to address the broader problem.

4.2. Geometrical Interpretation of the Velocity-Dependent Covering Fraction

To illustrate the importance of geometrical dilution, let the locus of fractures in a shell define individual clouds. Suppose, for simplicity, these clouds all have the same column density and initial velocity, equal to that of the shell just before blowout. If the area of a cloud does not change as it moves outwards (think of a brick-like cloud), then the covering fraction of clouds decreases as $C_f(R) = C_f(R_0)(R_0/R)^2$.

Most shell fragments are unlikely self-gravitating structures, however; and we expect them to expand as they fly outwards due to the drop in ambient pressure. The sound crossing time in a cloud is likely short enough for the cloud to maintain pressure equilibrium with the hot wind, $P_c \approx P_h$. The clouds expand adiabatically, so we can calculate their size at any outflow radius, R ,

⁶ Value of L_w from SB99 continuous star formation model (Leitherer et al. 1999) for $1 M_\odot \text{ yr}^{-1}$ in 1 to 100 M_\odot stars.

and compare the cloud area to the that of a solid shell, thereby estimating the covering fraction, $C_f(R)$.

Mass conservation in a steady-state, constant velocity hot wind requires the density to fall as $\rho_h \propto r^{-2}$. For an isothermal hot wind, the resulting increase in the volume of low-ionization clouds is

$$V_c(R) = \left(\frac{R}{R_0}\right)^{2/\gamma_c} V_c(R_0), \quad (15)$$

where $\gamma_c = 5/3$ for a monatomic, ideal gas. For roughly spherical clouds, the increase in cloud volume is accompanied by an increase in cloud area, $A_c \propto V_c^{2/3}$. Defining the covering fraction as

$$\frac{C_f(R)}{C_f(R_0)} = \frac{A_c(R)}{4\pi R^2} \frac{4\pi R_0^2}{A_c(R_0)}, \quad (16)$$

these relations yield a covering fraction,

$$\frac{C_f(R)}{C_f(R_0)} = \left(\frac{R}{R_0}\right)^{4/3\gamma_c-2}, \quad (17)$$

that falls as $R^{-1.2}$.

If the hot wind cools adiabatically, then $T_h \propto R^{-4/3}$, and the pressure falls off faster with radius. The lower pressure allows the clouds to expand faster than in the isothermal case. Repeating the steps in the previous paragraph, we find

$$\frac{C_f(R)}{C_f(R_0)} = \left(\frac{R}{R_0}\right)^{4\gamma_h/3\gamma_c-2}. \quad (18)$$

Assuming $\gamma = 5/3$ for both the hot wind and the clouds, we find

$$\frac{C_f(R)}{C_f(R_0)} = \left(\frac{R}{R_0}\right)^{-2/3}. \quad (19)$$

The low-ionization clouds cannot expand quickly enough to keep up with the geometrical dilution inherent to spherical, outflow geometry. Their covering fraction must decrease with increasing outflow radius.

4.3. Is Acceleration of the Low-Ionization Gas Required?

The absorption trough measurements require lower C_f at higher velocity. Geometrical dilution produces lower covering fractions at larger outflow radii. Combining these two results implies that the gas producing the highest velocity absorption resides at the largest distance from the starburst. While we find this argument illuminating, some of the underlying assumptions should be examined.

First, the outflow geometry is uncertain. It should be roughly spherical on spatial scales larger than the galaxy, but the outflow geometry may be better described as cylindrical at blowout. We know the absorbing gas lies close to the gaseous disk in some ULIRG outflows because the outflows present rotation in NaI (Martin 2006). In a version of the above model with cylindrical geometry, both the covering fraction and column density of 'brick-like' clouds become independent of height above the disk. The decrease in covering fraction would require

other physical effects such as cloud ionization, evaporation, or ablation to become important at the higher outflow velocities.

Second, blowout may yield a distribution of cloud column densities and velocities, something three-dimensional numerical simulations may soon be able to address. The fastest fragments – whether determined by blowout, acceleration by the hot wind, or acceleration by the starburst radiation – will reach the largest distances. Our models indicate the low-ionization cloud reach their maximum distance long after the starburst activity has ceased. It follows that if we observe such outflows during the starburst phase, the highest velocity absorption will come from material at the largest radii. Our underlying explanation for the shape of the absorption troughs would remain geometrical dilution; however, acceleration of the low-ionization outflow would not be required beyond blowout.

4.4. Measurement of Terminal Velocities and Estimates of Spatial Extent

Comparison of the MgII, MgI, and NaI absorption troughs indicates the highest velocity gas sometimes escapes detection in NaI and MgI. For example, in FSC0039-13, we detect MgI and NaI absorption to 300 km s⁻¹; but the MgII absorption demonstrates that the outflow persists to 500 km s⁻¹. In FSC1407+05, we measure terminal velocities of 350, 600, and 750 km s⁻¹ from NaI, MgI, and MgII, respectively. We find our spectral signal-to-noise ratio insufficient to detect the higher velocity components of these outflows in NaI and MgI.

The MgII lines allow more robust terminal velocity measurements for a number of reasons. First, the MgII 2796, 2803 transitions have a higher value of $N(X)/N_{Hf}$ than does NaI 5892, 5898. Second, expected ionization corrections favor singly-ionized Mg, Fe, and Na over their neutral species. Third, we find a larger cloud covering fraction for the singly-ionized lines than for neutral lines.

We emphasize that the highest velocity absorption detected in MgII appears to be limited by covering fraction. At continuum $SNR \sim 10$, the absorption trough blends with the continuum where $C_f(v) \lesssim 0.1$, regardless of column density. The gas at the largest radii may well go undetected by typical absorption-line measurements. For example, if we assume unity covering fraction at R_0 , then gas beyond $R \sim 3.2R_0$ cannot be detected if C_f falls as R^{-2} . In the more realistic case, $C_f \propto R^{-2/3}$, the covering fraction drops to 0.1 at $32R_0$. For a launch radius $R_0 \approx 200$ pc, our measurement would detect gas out to 6.4 kpc. This distance exceeds the extent of the H α filaments in many nearby starburst galaxies but remains considerably smaller than the recently detected soft, X-ray halos in ULIRGs (Sciortino & Martin, in prep.). Spectroscopy of background light sources at projected separations of just a few tens of kpc from starburst and post-starburst galaxies should be more effective than line-of-sight studies for determining the spatial extent of the low-ionization outflow, but such studies need to account for the geometrical dilution of the clouds.

5. SUMMARY AND CONCLUSIONS

We presented the first comparison of optical and near-ultraviolet absorption troughs in ULIRG spectra. We detected outflows in 5 ULIRGs in ground-state absorption from Na I, Mg I, Mg II, and Fe II. Previous observations of ULIRG outflows have been limited to the Na I doublet, and blending of the Na I 5890, 5896 lines complicated measurement of the absorption trough shape. We summarize the primary, empirical results.

- Comparison of the unblended, doublet components of Mg II and Fe II distinguish the effects of optical depth and covering fraction in determining the shape of the absorption troughs. The high optical depth in these transitions *at all outflow velocities* places a lower limit on the column density. The non-zero intensity requires partial coverage of the continuum source by the low-ionization gas over a broad velocity range.
- The covering fraction in all four ions decreases as the outflow velocity increases beyond the velocity of minimum intensity, or equivalently the velocity of maximum covering fraction. At a given velocity, the Mg I covering fraction is roughly half that measured in Mg II (and Fe II), and the covering fraction in Na I is less than or equal to that measured in Mg I.
- Accounting for these differences in ionic covering fraction, and taking spectral SNR into consideration, we detect Mg II, Fe II, Mg I, and Na I absorption over the same velocity range. The decrease in covering fraction with increasing velocity suppresses the absorption signature of the highest velocity gas. The higher covering fraction of Mg II (and Fe II) yields detection to higher velocity than indicated by Mg I (or Na I). Any comparison of terminal velocities measured from Na I and Mg II must take the bias introduced by the velocity-dependent covering fraction into consideration. Many measurements exist for Na I at $z \sim 0.6$, whereas ground-based, optical spectrographs can measure outflows with the Mg II doublet over the broad redshift range from ~ 0.25 to $z \sim 2.5$. Caution should be exercised when examining evolution in outflow properties between these samples. For completeness, we point out that our spectra do not cover high-ionization transitions like O VI 1032, 1038, which reveal higher-velocity gas in some starburst outflows (Grimes et al. 2009).
- The absence of Fe II* lines, principally the $\lambda 2612$ transition, place an upper limit on the volume density of $n_e < 10^{3.5} \text{ cm}^{-3}$, and likely $< 10^{3.1} \text{ cm}^{-3}$. When present in quasar outflows, low-ionization absorption troughs from excited or metastable states indicate much higher volume density $n_e = 10^{4.4} \text{ cm}^{-3}$ with less than 20% scatter (Korista et al. 2008; Arav et al. 2008). In the lower density ULIRG outflows, Mg II will be the dominant ionization state in the low-ionization outflow over a broad range of spectral hardness. In contrast, at these densities the Na I ionization fraction remains very sensitive to spectral hardness. We suggest that the

harder radiation field in dwarf galaxies likely explains the lower fraction of dwarf starburst outflows detected in Na I relative to ULIRGs, which are almost always detected in Na I (Martin 2005; Rupke et al. 2005b).

- We found Mg II emission in two Sey 2 ULIRGs and He I emission in all spectra.

These results provide new insight into the relationship of the low-ionization outflow and the hot wind. We defer physically-motivated models of the absorption trough shape to another paper (Martin 2009, in preparation)) but summarize key aspects of the emerging, physical picture here.

- We associate the velocity of maximum covering fraction with that of a swept-up shell of interstellar gas at the time of blowout. Factors motivating this interpretation include the Doppler shift of the trough minimum (0 to -400 km s^{-1}), the large width of the absorption troughs (up to 800 km s^{-1}), the column density lower limits, and results from recent numerical simulations (Fujita et al. 2009). Regardless of their physical origin, however, the large velocity width of the absorption troughs require contributions from multiple structures along the sightline. The relative shapes of the doublet troughs require these clouds or filaments to transition sharply (spatially) from opaque to optically thin gas. The neutral alkali metals reside in the same kinematic structures as the singly ionized metals but fill a smaller fraction of that volume.
- The most significant result of our study may be the discovery of a velocity-dependent covering fraction in low-ionization outflows. The simplest interpretation is geometrical. The dilution associated with the spherical expansion of a population of absorbers causes their covering fraction to decrease with increasing radius. We showed that the adiabatic expansion of clouds in pressure equilibrium with the hot wind is not fast enough to offset this dilution. *In the context of this physical scenario, our result implies that the high-velocity gas detected in the absorption trough is at larger radii than the lower velocity (and higher covering fraction) gas.* This mapping between velocity and relative radius indicates allows requires acceleration of the low-ionization gas. Either shell blowout or subsequent momentum-driving by a hot wind and/or radiation pressure could cause this acceleration.
- In an alternative scenario, the shell fragments into clouds with a wide range of column densities. Due to momentum conservation, the ram pressure of the hot wind (or radiation pressure) would accelerate the lowest column density fragments to the highest terminal velocities. This relationship might even arise from blowout alone without requiring a momentum-driven wind phase. Either way, the new empirical constraint, requiring lower covering fraction at higher velocity, would imply the covering fraction of low-ionization gas increases with

increasing column density. We find the first, geometrical explanation more appealing due to its simplicity.

- The lower limits on NaI and FeII column density provide the highest (i.e. strongest) lower limits on the mass outflow rate in low-ionization gas. Better limits can be obtained by either determining the NaI ionization fraction or observing bluer, FeII transitions with lower oscillator strengths.
- Assuming that photoionization equilibrium likely sets the temperature of the low-ionization outflow, $T_e \sim 10^4$ K, the upper limit on the volume density allows the pressure of the cold outflow to be as high as $P_c/k \lesssim 10^7$ K cm⁻³. Tighter constraints on the volume density would be valuable, as very low density would be incompatible with pressure equilibrium with a hot wind, $P_c \approx P_h$, and favor a purely radiatively-driven outflow.

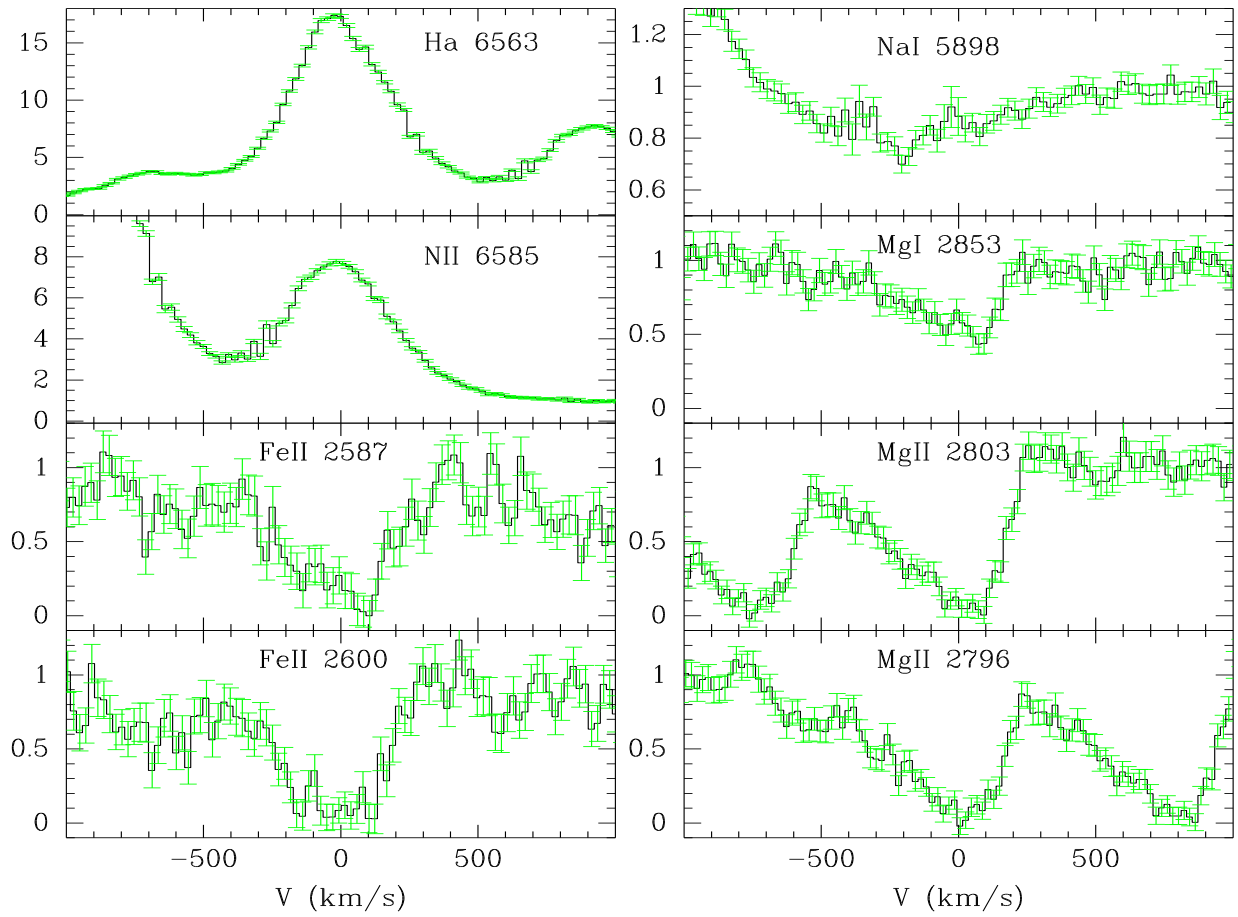
Our conclusion about the acceleration of the low-ionization outflow, while illustrative, is subject to an assumption about outflow geometry and a bias towards a shell origin for the low-ionization gas. Our empiri-

cal results, however, clearly challenge plausible dynamical models. Acceptable models need to reproduce the velocity-dependence of the low-ionization covering fraction, explain the lower covering fraction of neutral, alkalai metals relative to low-ionization species, and be consistent with the observed constraints on both column density and volume density. With sufficient spectral sensitivity, all of these outflow properties can be measured over a very broad redshift range, so we expect any evolutionary effects with galaxy mass and/or cosmic time to eventually be measured.

We thank Nahum Arav, Tim Heckman, and Peng Oh for useful discussions regarding the interpretation of these data. We thank Doug Edmonds for making his number density diagnostics available to us and an anonymous referee for insightful comments. Special thanks to Amiel Sternberg for his assistance in setting up STARS with the UVBlue stellar library. This work was supported by the National Science Foundation under contract 080816, the David and Lucile Packard Foundation, and the Aspen Center for Physics.

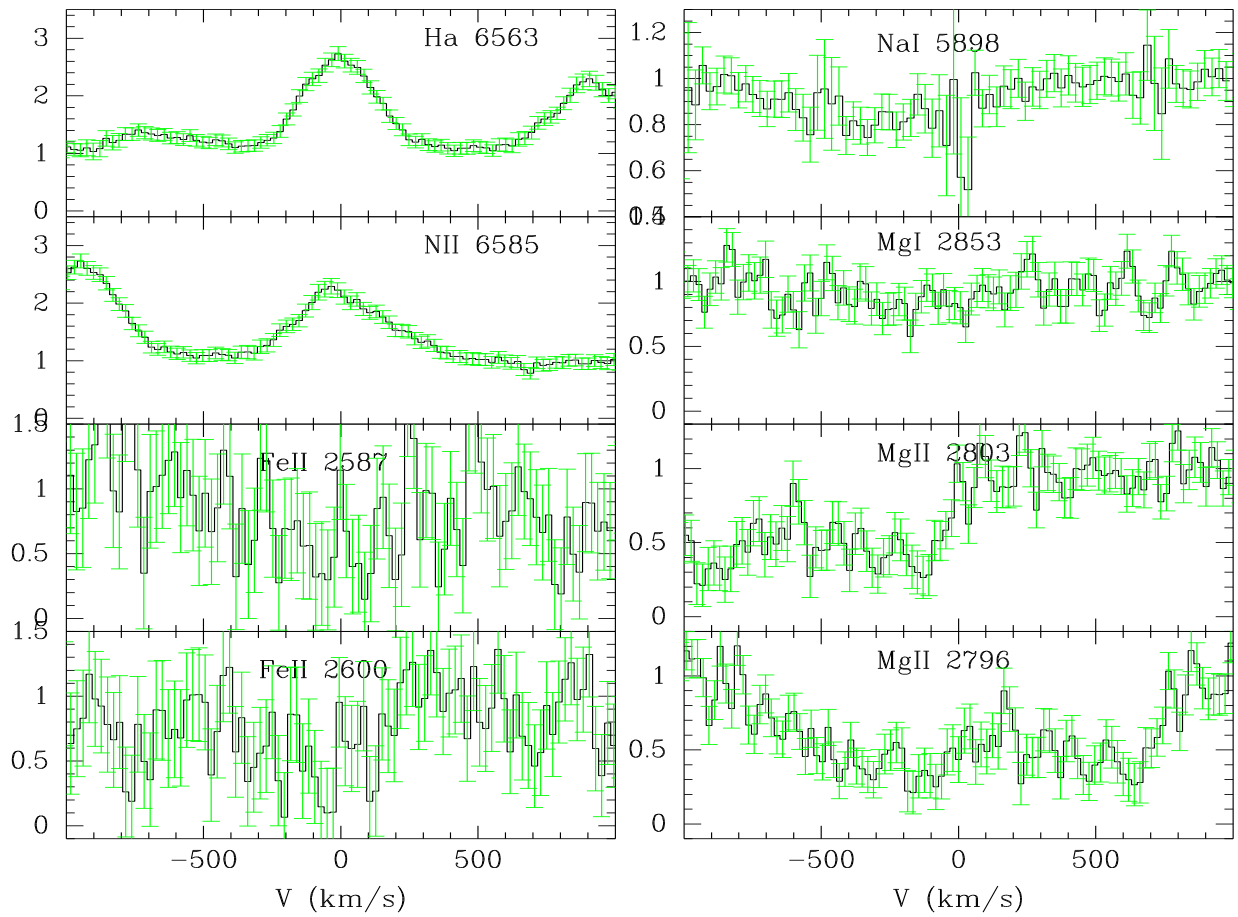
REFERENCES

- Arav, N. et al. 1999a, ApJ, 516, 27
 Arav, N. et al. 2008, ApJ, 681, 954
 Arav, N. et al. 2005, ApJ, 620, 665
 Arav, N. et al. 2001, ApJ, 546, 140
 Borne, K. D. et al. 2000, ApJ, 529, L77
 Breitschwerdt, D. 2008, Nature, 452, 826
 Cooper, J. L. et al. 2008, ApJ, 674, 157
 Dahlem, M., Weaver, K. A., & Heckman, T. A. 1998, ApJ, 118, 401
 Davies, R. I. et al. 2007, ApJ, 671, 1388
 DeYoung, D. S. & Heckman, T. M. 1994, ApJ, 431, 598
 de Kool, M. et al. 2002, ApJ, 580, 54
 Everett, J. et al. 2008, ApJ, 674, 258
 Fujita, A. et al. 2009, ApJ, 698, 693
 Gabel, J. R. et al. 2003 ApJ, 583, 178
 Grimes, J. P. et al. 2009, ApJS, 181, 272
 Hanuschik, R. W. 2003, A&A, 407, 1157
 Heckman, T. et al. 1990, ApJS, 74, 833
 Heckman, T., Lehnert, M. D., Strickland D. K., & Lee, A. 2000, ApJS, 129, 493
 Hoopes, C. G. et al. 2005, ApJ, 619, L99
 Kennicutt, R. C. 1989 ApJ, 344, 685 [K89]
 Kewley, L. J. et al. 2006, MNRAS, 372, 961
 Kim, D. C. et al. 1998b ApJ, 508, 627
 Kim, D.-C. & Sanders, D. B. 1998, ApJS, 119, 41 [KS98]
 Kim, B.-C. et al. 2002, ApJS, 143, 277
 Korista, K. T. et al. 2008, ApJ, 688, 108
 Leitherer, C. 1999, ApJS, 123, 3
 Le Floc'h, E. et al. 2005, ApJ, 632, 169
 Mac Low, M.-M., McCray, R., & Norman, M. L. 1989, ApJ, 337, 141
 Marcolini, A. et al. 2005, MNRAS, 362, 626
 Martin, C. L. 1998, ApJ, 506, 222
 Martin, C. L. 1999, ApJ, 513, 156
 Martin, C. L. 2005, ApJ, 621, 227
 Martin, C. L. 2006, ApJ, 647, 222
 Martin, C. L., Kobulnicky, H. A., Heckman, T. M. 2002, ApJ, 574, 663
 McCarthy, J. K., Cohen, J. G., Butcher, B., Cromer, J., Croner, E., Douglas, W. R., Goeden, R. M., Grewal, T., Lu, B., Petrie, H. L., Weng, T., Weber, B., Koch, D. G., & Rodgers, J. M. 1998 SPIE, 3355, 81
 McKee, C. F. & Ostriker, J. P. 1988, RvMP, 60, 1
 Morton, D. C., 1991, ApJS, 77, 119
 Morton, D. C., 2003, ApJS, 149, 205
 Murray, N. Martin, C. L, Quataert, E & Thompson, T. A. 2007, ApJ, 660, 211
 Murray, N., Quataert, E., & Thompson, T. A. 2005, ApJ, 618, 569
 Oke, J. B., Cohen, J. G., Carr, M., Cromer, J., Dingizian, A. & Harris, F. H. 1995, PASP, 107, 375
 Oppenheimer & Davé 2006, ApJ, 373, 1265
 Rodríguez-Merino, L. H., Chavez, M., Bertone, E., & Buzzoni, A. 2005, ApJ, 626, 411
 Rupke, D. S., Veilleux, S., & Sanders, D. B. 2002, ApJ, 570, 588
 Rupke, D. S., Veilleux, S., & Sanders, D. B. 2005a, ApJS, 160, 87
 Rupke, D. S., Veilleux, S., & Sanders, D. B. 2005b, ApJS, 160, 115
 Rupke D., Veilleux, S., & Sanders, D. B. 2005d, ApJ, 632, 751
 Sanders, D. B. et al. 1988, ApJ, 328, 35
 Sanders, D. B. & Mirabel, F. 1996 ARA&A34, 725
 Savage, B. D. & Sembach, K. R. 1996, ARA&A, 34, 279
 Sato, T. et al. 2009, ApJ, 696, 214
 Schwartz, C. S. & Martin, C. L. 2004, ApJ, 610, 20
 Scott, J. E. 2004, ApJS, 152, 1
 Shapley, A. E. et al. 2003, ApJ, 588, 65
 Shopbell, P. L. & Bland-Hawthorne, J. 1998, ApJ, 493, 129
 Shull, M. 1993, in ASP Conf. Proceedings 35, Massive Stars: Their Lives in the Interstellar Medium, ed. J. P. Cassinelli & E. B. Churchwell (San Francisco: ASP), 327
 Shull, J. M. & Van Steenberg, M. 1982, ApJS, 48, 95
 Socrates, A., Davis, S. W., & Ramirez-Ruiz, E. 2008, ApJ, 687, 202
 Somerville, R. S. & Primack, J. R. 1999, MNRAS, 310, 1087
 Sternberg, A. 1998, ApJ, 506, 721
 Sternberg, A., Hoffmann, T. L. & Pauldrach, A. W. A. 2003, ApJ, 599, 1333
 Strickland, D. K. et al. 2002, ApJ, 568, 689
 Tenorio-Tagle, G., & Bodenheimer, P. 1988, ARA&A, 26, 145
 Thornley, M. D. et al. 2000, ApJ, 539, 641
 Veilleux, S. et al. 1999, ApJ522, 113
 Veilleux, S. et al. 2002, ApJS, 143, 315
 Veilleux, S. et al. 2006, ApJS, 643, 707
 Veilleux, S. et al. 2009a, ApJS, 182, 628
 Veilleux, S. et al. 2009b, ApJ, 700, 149
 Walter, F., Weiss, A., & Scoville, N. 2002, ApJ, 580, 21
 Weaver, R. et al. 1977, ApJ, 218, 377
 Weiner, B. J. et al. 2009, ApJ, 692, 187



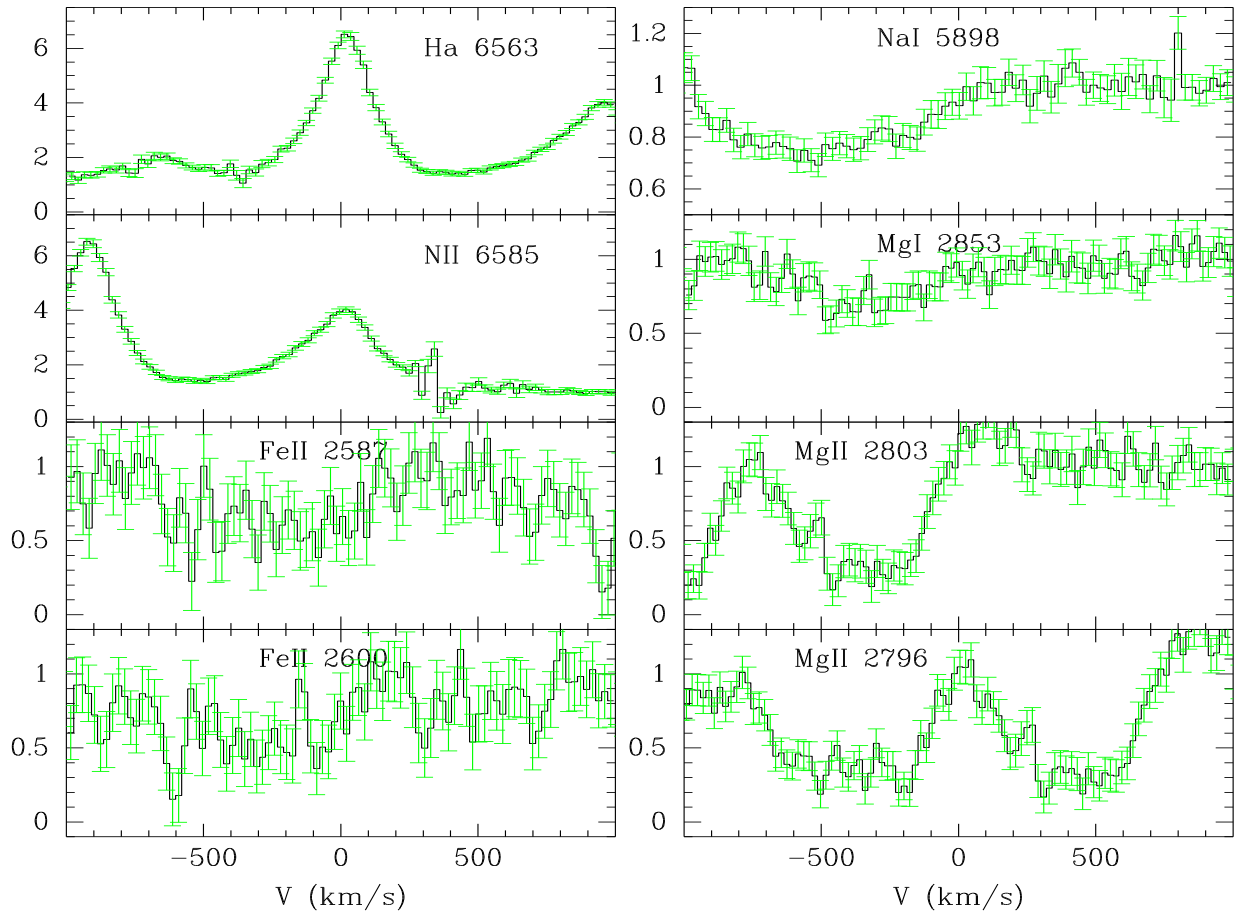
(a) LRIS spectra of FSC0039-13

FIG. 1.— Normalized intensity vs. velocity, where the velocity is relative to the systemic velocity determined from emission lines.



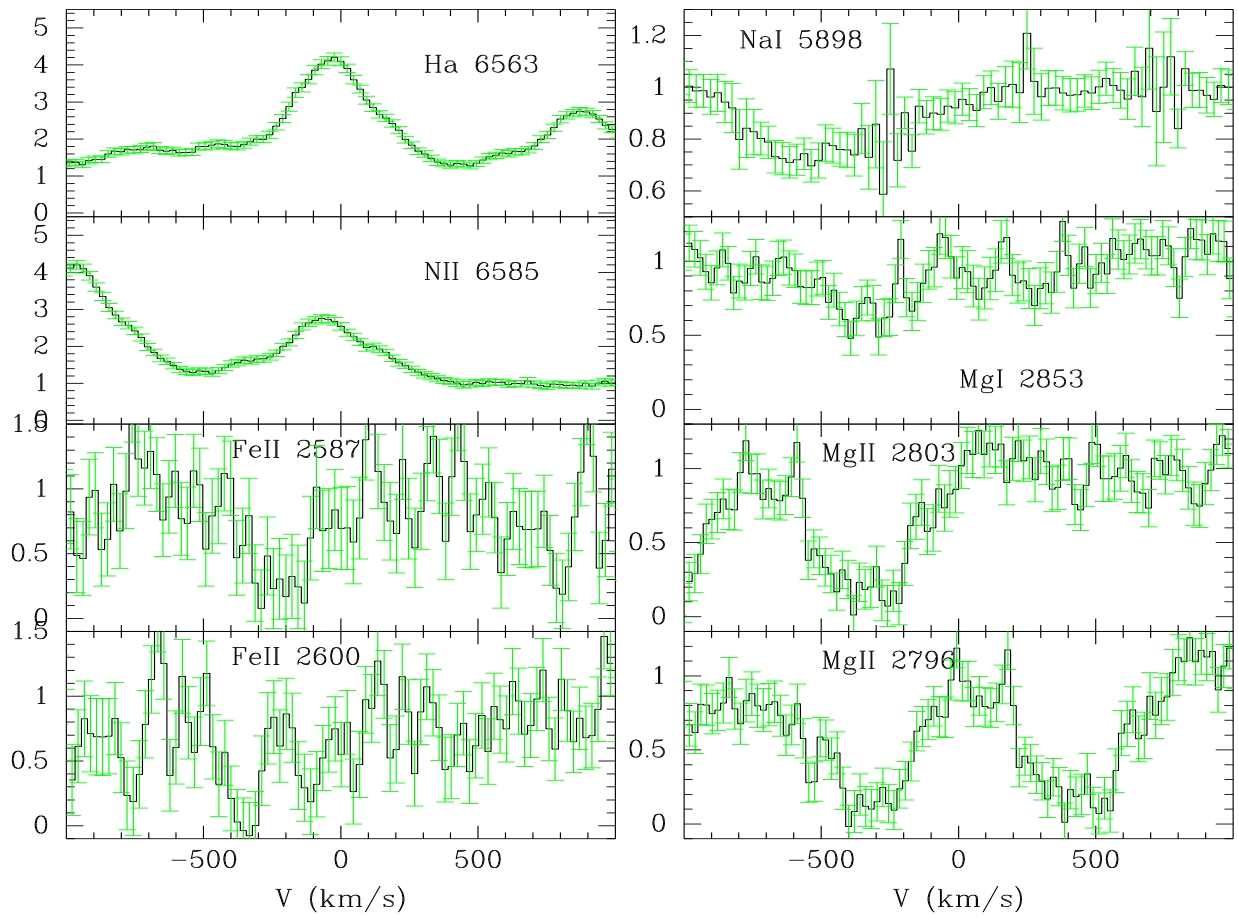
(b) LRIS spectra of FSC1009+47

FIG. 1.— continued



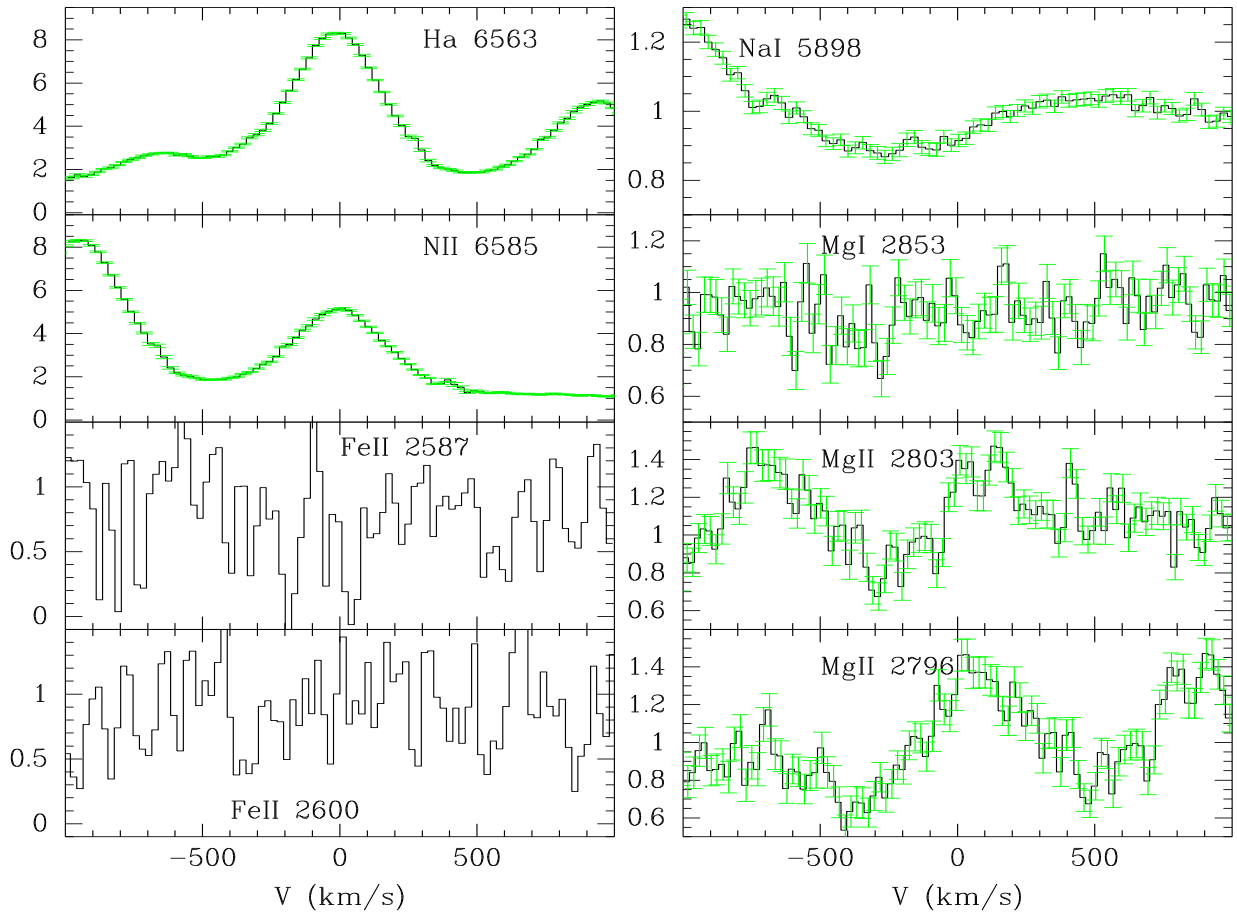
(b) LRIS spectra of FSC1407+05

FIG. 1.— continued



(b) LRIS spectra of FSC1630+15

FIG. 1.— continued



(b) LRIS spectra of FSC2349+24

FIG. 1.— continued

TABLE 1

Object	f25/f60	f60/f100	Spectral Type	$\log(L_{IR}/L_{\odot})$	SFR-S ($M_{\odot} \text{ yr}^{-1}$)	SFR-C ($M_{\odot} \text{ yr}^{-1}$)
(1)	(2)	(3)	(4)	(5)	(6)	(7)
FSC00397-1312	0.180	0.963	HII (V99)	12.81	1110	653
FSC10091+4704	0.068	0.761	LINER(V99,K98b)	12.57	641	377
FSC14070+0525	0.131	0.797	Sey2 (K98b)	12.66	789	464
FSC16300+1558	0.047	0.744	LINER (K98b)	12.53	585	344
FSC23498+2423	0.118	0.703	Sey2 (V99)	12.31	352	207

NOTE. — (1) ULIRG name. (2) f25/f60 color computed from far-infrared fluxes in KS98. (3) f60/f100 color computed from far-infrared fluxes in [KS98]. (4) Spectral type from Kim et al. (1998b) – FSC1009+47, FSC1407+05, FSC1630+15, – and Veilleux et al. (1999) – FSC0039-13, FSC1009+47, FSC2349+24. (5) L_{IR} calculated using the prescription of Sanders & Mirabel (1996). For FSC objects, the luminosities from Kim et al. (2002) and Veilleux et al. (1999), which assume luminosity distances based on $H_0 = 75 \text{ km s}^{-1} \text{ Mpc}^{-1}$ and $q_0 = 0$, were converted to the cosmology used throughout this paper. (6) For Salpeter IMF from 0.1 to $100 M_{\odot}$, the star formation rate is $SFR = L_{IR}/5.8 \times 10^9 L_{\odot}$, where L_{IR} is the bolometric luminosity (Kennicutt 1989). (7) SFR for Chabrier IMF, i.e. K89 SFR by 1.7.

TABLE 2

Object	Redshift	PA (deg)	Res. (km/s)	SNR	Date Observed	Notes
(1)	(2)	(3)	(4)	(5)	(6)	(7)
FSC00397-1312	0.26171	-54.0	160	9.4	2007 Nov. 1	Advanced Merger
FSC10091+4704	0.24508	168.0	130	5.0	2004 Jan. 26, Mar. 16-17	Diffuse Merger
FSC14070+0525	0.26602	-25.0	110	8.2	2004 Jan. 26, Mar. 16-17	Advanced Merger
FSC16300+1558	0.24200	-45.0	155	6.2	2004 Mar. 16-17, 2007 Oct. 6	Pre-Merger, Separation 4.4 kpc
FSC23498+2423	0.21249	-45.9	160	6.4	2007 Nov. 1	Pre-Merger, Separation 14 kpc

NOTE. — (1) Target. (2) Redshift measured from emission lines including $H\alpha$, [NII] 6584,48, [SII] 6717,31, and [OI] 6300,64. The absolute velocities have not been corrected to the Local Standard of Rest. (3) Position angle of the longslit measured east of north. (4) Spectral resolution defined by the measured full width at half maximum intensity of the arc lamp lines. If frames from different runs are combined, then the poorer of the two resolutions is listed. (5) SNR per pixel is measured in a 100\AA bandpass immediately blueward of MgII. (6) Date(s) observed. (7) The Veilleux et al. (2002) merger classification is compared to the structure observed along the longslit.

TABLE 3
FITTED COVERING FRACTIONS

FSC (1)	V(km/s) (2)	$C_f(\text{MgII})$ (3)	$\tau_0(2803)$ (4)	$\chi^2_{\nu}(\text{MgII})$ (5)	$C_f(\text{MgI})$ (6)	$\tau_0(2853)$ (7)	$\chi^2_{\nu}(\text{MgI})$ (8)	$C_f(\text{NaI})$ (9)	$\tau_0(5898)$ (10)	$\chi^2_{\nu}(\text{NaI})$ (11)	$C_f(\text{FeII})$ (12)	$\tau_0(2587)$ (13)	$\chi^2_{\nu}(\text{FeII})$ (14)
0039-13	83	0.74 ± 0.03	17.7	1.136	0.41 ± 0.22	4	1.417	0.17 ± 0.02	4	2.335	0.99 ± 0.04	2.8	2.452
0039-13	-2.6	0.83 ± 0.03	17.7	1.136	0.57 ± 0.38	4	1.417	0.04 ± 0.02	4	2.335	0.90 ± 0.05	2.8	2.452
0039-13	-135	0.47 ± 0.06	17.7	1.136	0.20 ± 0.08	4	1.417	0.11 ± 0.02	4	2.335	0.72 ± 0.05	2.8	2.452
0039-13	-209	0.45 ± 0.05	17.7	1.136	0.24 ± 0.07	4	1.417	0.05 ± 0.02	4	2.335	0.50 ± 0.06	2.8	2.452
0039-13	-379	0.33 ± 0.02	17.7	1.136	0.19 ± 0.04	4	1.417	0.09 ± 0.01	4	2.335	0.31 ± 0.04	2.8	2.452
0039-13	-571	0.27 ± 0.02	17.7	1.136	0.21 ± 0.03	4	1.417	0.07 ± 0.01	4	2.335	0.43 ± 0.04	2.8	2.452
1009+47	-104	0.66 ± 0.05	5	0.955	0.17 ± 0.11	3.4	1.243	0.16 ± 0.05	3	0.372
1009+47	-361	0.55 ± 0.05	5	0.955	0.11 ± 0.08	3.4	1.243	0.08 ± 0.05	3	0.372
1009+47	-239	0.51 ± 0.05	5	0.955	0.25 ± 0.10	3.4	1.243	0.17 ± 0.04	3	0.372
1009+47	-507	0.51 ± 0.04	5	0.955	0.07 ± 0.07	3.4	1.243	0.02 ± 0.04	3	0.372
1009+47	-692	0.38 ± 0.04	5	0.955	0.10 ± 0.06	3.4	1.243	0.04 ± 0.06	3	0.372
1407+05	-89	0.29 ± 0.04	10	0.989	0.16 ± 0.08	6.8	1.045	0.11 ± 0.02	3	0.702	0.52 ± 0.07	1.6	1.232
1407+05	-187	0.40 ± 0.07	10	0.989	0.08 ± 0.07	6.8	1.045	0.10 ± 0.02	3	0.702	0.14 ± 0.11	1.6	1.232
1407+05	-265	0.62 ± 0.04	10	0.989	0.28 ± 0.09	6.8	1.045	0.17 ± 0.02	3	0.702	0.55 ± 0.08	1.6	1.232
1407+05	-434	0.67 ± 0.04	10	0.989	0.37 ± 0.05	6.8	1.045	0.20 ± 0.01	3	0.702	0.49 ± 0.07	1.6	1.232
1407+05	-615	0.51 ± 0.03	10	0.989	0.15 ± 0.04	6.8	1.045	0.14 ± 0.02	3	0.702	0.59 ± 0.07	1.6	1.232
1630+15	-114	0.28 ± 0.05	5	1.086	0.10 ± 0.09	3.4	1.014	0.13 ± 0.03	3	0.491
1630+15	-252	0.81 ± 0.05	5	1.086	0.24 ± 0.12	3.4	1.014	0.21 ± 0.03	3	0.491
1630+15	-362	0.82 ± 0.05	5	1.086	0.42 ± 0.14	3.4	1.014	0.16 ± 0.04	3	0.491
1630+15	-491	0.60 ± 0.05	5	1.086	0.22 ± 0.07	3.4	1.014	0.12 ± 0.03	3	0.491
1630+15	-676	0.21 ± 0.04	5	1.086	0.08 ± 0.05	3.4	1.014	0.07 ± 0.04	3	0.491
2349+24	-71	0.27 ± 0.03	2	2.247	0.12 ± 0.07	1.4	2.254	0.08 ± 0.007	5	4.259
2349+24	-182	0.28 ± 0.03	2	2.247	0.04 ± 0.05	1.4	2.254	0.05 ± 0.007	5	4.259
2349+24	-298	0.38 ± 0.03	2	2.247	0.30 ± 0.07	1.4	2.254	0.02 ± 0.007	5	4.259
2349+24	-423	0.27 ± 0.03	2	2.247	0.27 ± 0.06	1.4	2.254	0.02 ± 0.007	5	4.259
2349+24	-591	0.17 ± 0.03	2	2.247	0.17 ± 0.05	1.4	2.254	0.008 ± 0.007	5	4.259

NOTE. — (1) Galaxy. (2) Doppler shift of component in km s^{-1} . All components have a Doppler parameter $b \equiv 50 \text{ km s}^{-1}$, or $b_{50} \equiv 1$. (3) Fitted covering fraction for MgII (4) Minimum optical depth at line center for MgII 2803. The lower limit on the ionic column density is $N(\text{MgII}) > 3.90 \times 10^{13} \text{ cm}^{-2} \tau_0 b_{50}$. (5) Fit statistic for the MgII doublet. (6) Fitted covering fraction for MgI (7) Minimum optical depth at line center for MgI 2853. The lower limit on the ionic column density is $N(\text{MgI}) > 6.39 \times 10^{12} \text{ cm}^{-2} \tau_0 b_{50}$. (8) Fit statistic for the MgI line. (9) Fitted covering fraction for NaI. (10) Minimum optical depth at line center for NaI 5898. The lower limit on the ionic column density is $N(\text{NaI}) > 1.78 \times 10^{13} \text{ cm}^{-2} \tau_0 b_{50}$. (11) Fit statistic for the NaI doublet. (12) Fitted covering fraction for FeII. (13) Minimum optical depth at line center for FeII 2600. The lower limit on the ionic column density is $N(\text{FeII}) > 1.87 \times 10^{14} \text{ cm}^{-2} \tau_0 b_{50}$. (14) Fit statistic for the FeII doublet.